MAGMONS:

Solitary Waves Arising in the Buoyant Ascent of Magma by Porous Flow Through a Viscously Deformable Matrix

Thesis by

David Russell Scott

In Partial Fulfillment of the Requirements
of the Degree of Doctor of Philosophy

California Institute of Technology
Pasadena, California

1987

(submitted 8th January, 1987)

Acknowledgements

My interest in the physical modelling of igneous processes was inspired by Don Anderson. It is my good fortune that Dave Stevenson was already interested in the idea and agreed to act as my guide. Many individuals at the Division of Geological and Planetary Sciences have shown interest and provided encouragement and technical assistance, particularly Huw Davies, Brad Hager, Ann Mori, Oded Navon, Mike O'Hara, Arthur Raefsky, Sally Rigden-Hill, Ed Stolper, Bob Svendsen, Gerry Wasserburg, and Steve Wickham. Rob Clayton and his system managers have been very forgiving of my occasional appetite for computer time. The interest of a number of people outside Caltech has improved both the quality of the work I present here and my sense of scientific discipline: Andrew Fowler, Dan McKenzie, Peter Olson, Neil Ribe, Frank Richter, and Jack Whitehead. It was an honor to receive a Gutenberg fellowship from the Seismological Laboratory for my first year. Subsequently I was supported by the National Science Foundation through Professors Kanamori, Hager, and Stevenson.

I am deeply grateful for the friendship and tolerance of all those with whom I have lived, worked, and relaxed during my stay, especially to Ann Mori, David Pickett, Leslee Holderness, and Tom Hearn. My family have remained loyal and loving during my absence, and it is to them that I dedicate this thesis.

From a letter by Sir Joseph Prestwich, then Professor of Geology at Oxford, to the Reverend Osmond Fisher, 28th March 1878:

> "*No hypothesis, it seems to me, meets all the conditions of geological phenomena so well . . . as that of the original fluidity of the globe, and I think that none meets the present condition of volcanic and earthquake disturbances so well as that the solidification is not yet thoroughly complete, though the remaining quantity of fluid matter is not such as to interfere with the rigidity required . . .*"

From a letter by Prestwich to Sir John Evans, 22nd October 1893:

> "*. . . any child could see that volcanic action is spasmodic, and has always been so.*"

Abstract

The dynamics of partially molten regions of the Earth's mantle are studied using a combination of theoretical, experimental, and numerical techniques. The physical model is based on experimental observations of partially molten ultramafic rocks and incorporates two elements: buoyancy-driven porous flow of magma through a viscously deformable matrix, and buoyancy-driven circulation of the whole rock.

The first element of this model is analogous to buoyancy-driven pipe flow of a liquid through a denser and more viscous wall fluid. Laboratory experiments on this system illustrate the phenomenon of solitary waves. These are waves of larger pipe radius that ascend a uniform pipe of smaller radius. The waves are very nearly conserved in collisions. These, and the corresponding waves of higher porosity that arise in one-dimensional porous flow, are characterized further by analysis and numerical experiments.

The full system, incorporating circulation in a multidimensional porous medium, also displays solitary waves governed by the same basic processes as the one-dimensional waves. Analysis and numerical experiments show that the multidimensional waves have a circular or spherical form.

A possible natural manifestation of this fluid dynamical phenomenon is in igneous processes. Magmons, as the waves are called in that setting, probably have wavelengths of kilometers and velocities of centimeters per year. Magma ascent in magmons may account for episodicity in igneous emplacement. Also, a magmon can collect and mobilize a small degree of partial melt without disturbing its geochemical signature. In a partially molten region the characteristic wavelength of magmons will always be superimposed on that of large scale variations in porosity.

Table of Contents

Chapter 4:

Introduction

Prestwich's [1885] early view of the causes of "volcanic action" is probably incorrect, but in a philosophical sense his work has a great deal in common with this thesis. Like him, we identify a series of processes that lead to the emplacement of igneous rocks.

His primary process is the contraction of the cooling earth, squeezing out liquids that remain from the Earth's original molten state. With the insight afforded by the framework of plate tectonics, we see that the liquids do not need to be primordial, but instead that melting can occur at the present due to mantle convection. The magma must then ascend and segregate from its parent rock by processes that result in emplacement of the magma at or near the earth's surface. Experimental observations of ultramafic rocks [Waff and Bulau, 1979; Vaughan *et al.*, 1982] show that the liquid can form an interconnected network within the crystalline matrix; the liquid could therefore flow relative to the matrix. This has motivated us to regard buoyancy-driven porous flow as the initial transport process leading to melt segregation.

Other transport processes will doubtless take over at later times. In particular, transport through the brittle lithosphere probably occurs through cracks [Weertman, 1971; Shaw, 1980; Stevenson, 1983; Spera, 1984; Spence and Turcotte, 1985]. Incidentally, Prestwich emphasizes the role of water in this secondary stage, and indeed the exsolution of volatiles is discussed in the more recent references.

The porous flow process is particularly interesting because the melt is in intimate contact with the matrix through which it is flowing. The geochemical signature acquired by the melt during porous flow may be observable; in particular, it may be distinct from the signatures of higher level processes involving larger conduits or magma chambers, where fractional crystallization will dominate. It is the body of modern geochemical data that gives us a prospect of constraining our physical models of magma ascent and segregation.

The novel ingredient in our physical models is the dynamic deformation and compaction of the matrix in response to the flow of the liquid. This has received a considerable amount of attention in the last few years [McKenzie, 1984; Richter and McKenzie, 1984; Scott and Stevenson, 1984, Scott and Stevenson, 1986; Fowler, 1985; Ribe, 1985, and others]. Because porous flow is the primary transport process, melting of the parent rock may be occurring at the same time. In different settings, either the melting rate or the transport process may be the rate-limiting factor in magma supply. In the former case, the compaction process is unimportant, and the familiar form of Darcy's law is an adequate description of the porous flow. In the latter case, Darcy's law must be modified to include the effect of matrix deformation. In recent studies of this system [Scott and Stevenson, 1984; Richter and McKenzie, 1984], solitary wave solutions have been identified, consisting of localized regions of high porosity that ascend through the porous matrix.

The focus of this thesis is on the characterization of these solitary waves, which we call "magmons." Experimental, numerical, and analytic techniques are employed. Considerable attention is also paid to the derivation of the governing equations. In an attempt to clarify this derivation, we develop first a simple but precise model of pipe flow, in Chapter 1, and then a complete model of porous flow, in Chapter 2.

Most of the text and figures presented here are drawn from four published papers:

Stevenson, D. J., and D. R. Scott, Melt migration in deformable media, NATO ASI Series, Proceedings of the Workshop on the Structure and Dynamics of Partially Solidified Systems, in press, 1987.

Scott, D. R., and D. J. Stevenson, Magma ascent by porous flow, *J. Geophys.*

Res., **91**, 9283-9296, 1986.

Scott, D. R., D. J. Stevenson, and J. A. Whitehead, Jr., Observations of solitary waves in a viscously deformable pipe, *Nature*, **319**, 759-761, 1986.

Scott, D. R., and D. J. Stevenson, Magma solitons, *Geophys. Res. Lett.*, **11**, 1161-1164, 1984.

In addition, a substantial body of new work is presented in Chapters 2 and 4; this will be submitted subsequently for publication. In preparing this thesis I have taken the opportunity to edit and rearrange the material listed above. This has, amongst other things, eliminated some redundancy.

Chapter 1 introduces the fluid dynamical concepts on which all this work is based. These, and the most important results, are illustrated by a simple laboratory experiment.

Chapter 2 is devoted to the development of the complete mathematical model of buoyancy-driven porous flow, viscous compaction, and circulation in a partially molten rock. A substantial part of the derivation and discussion of the model is unpublished.

Chapter 3 explores the behavior expected of magmons in the Earth. A mixture of analysis and numerical modeling build an understanding of the phenomenon, and the possible consequences of magma ascent in magmons are discussed.

Chapter 4 concentrates on the numerical modeling and analysis of porous flow and compaction in two dimensions and three dimensions with axisymmetry. This chapter contains the remaining unpublished work, on the competition between porous flow and circulation.

CHAPTER 1

OBSERVATIONS OF SOLITARY WAVES IN A VISCOUSLY DEFORMABLE PIPE

An Introduction to Two-Phase Flow and Compaction

Abstract

We have made simple observations of the ascent of a buoyant fluid through a pipe formed in a denser and more viscous fluid that can deform viscously, allowing the pipe radius to change. There is no wall between the two fluids, and the Reynolds number is small in both fluids. If the buoyant fluid is supplied at a uniform rate, the system exhibits uniform Poiseuille flow. The response of the system to fluctuations in the rate of supply of the buoyant fluid is to form local maxima in the pipe radius that ascend as solitary waves. Larger amplitude waves can catch up and collide with smaller waves, and to a good approximation both waves recover their original form and amplitude after such a collision. Periodic wave trains are formed when the supply of fluid to the pipe is increased and sustained at a higher rate. These observations gain significance because the system is analogous to that of buoyancy-driven porous flow in a viscous matrix. The experiment may be regarded as a laboratory analogue for studying some aspects of the equations governing porous flow. The observed

behavior is consistent with theoretical and computational studies described in the subsequent chapters, which focus on the problem of magma migration in the earth. The behavior we observe will, however, arise in other systems governed by the same mechanics. The existence of solitary waves in such systems means that the responses to transient changes in the porosity or the supply of fluid could be long-lived.

Introduction

Our interest in this system arises from recent advances [McKenzie, 1984] in the understanding of the segregation of magma from a porous matrix of residual crystals, an important process in the crust and mantle of the earth. Observations of the texture of partially molten rocks [Waff and Bulau, 1979] have shown that the network of melt may remain interconnected down to very small volume fractions of melt. Recent work identifies the importance of compaction: the deformation of the porous matrix through which the buoyant melt rises. This work has prompted the formulation of a system of equations governing the movement of a buoyant fluid through a porous, deformable matrix; the latter property is essential if magma is to escape from a closed region of partial melt. Our experiment reproduces the essential mechanics of the more complex porous flow problem and is of interest to those studying porous systems other than partially molten rock.

Description of the Experiment

The experimental apparatus is very simple and can be reproduced easily and inexpensively. A transparent tank, approximately 10 cm x 10 cm x 50 cm high, contains transparent viscous fluid. This fluid forms the walls of the deformable pipe. To form the pipe, a buoyant fluid that is less viscous is introduced through a nozzle in the center of the base of the tank. This fluid is supplied from a reservoir with a variable pressure head, or by a low-rate pump such as a syringe driver. The buoyant fluid is dyed to make the pipe clearly visible. The experimental fluids we have used are different mixtures of clear honey and water. Diluting honey with water produces a mixture that is less dense and less viscous than pure honey. In the figures shown here, the denser fluid in the tank is 100% honey (density 1.42 g/cm^3, viscosity 80 Poise), and the buoyant fluid in the pipe is 77% honey (density 1.31 g/cm^3, viscosity 0.6 Poise). The use of mutually soluble fluids eliminates the effects of surface tension. We have determined that diffusion of water between the two fluids is negligible in the experiment. The use of different mixtures of corn syrup and water also provides good results.

The first of the buoyant fluid to be introduced ascends as a diapir, but as more fluid is supplied a pipe is established between the nozzle and the top of the tank [Whitehead and Luther, 1985]. If the pressure head of the reservoir of buoyant fluid is held constant, a state of steady Poiseuille flow is established. In this state the pressure head almost balances the resistance in the tubing supplying the nozzle because the Reynolds number is small, so there is no pressure difference between the two fluids in the tank. Within the pipe, the buoyancy force balances the non-hydrostatic pressure gradient. We typically use pipe diameters of a millimeter or two.

To create solitary waves, the rate of supply of fluid to the stable pipe must be increased. This can be achieved by increasing the pressure head of the reservoir or by increasing the supply rate from the syringe driver. In our experiments, the pipe has invariably responded to the change in supply rate by forming solitary waves or wave trains.

If the increased supply is temporary, followed by a return to the original rate, solitary waves are formed. With care, it is possible to form a single solitary wave. The solitary wave ascends along the uniform pipe at a constant velocity, with unchanging form. The pipe returns to its original uniform diameter after the passage of the wave. Although the waves are shape-preserving, they are dispersive in that they have an amplitude-dependent phase velocity. A consequence of this is that larger waves catch up and collide with smaller waves; the remarkable observation is that both waves survive such a collision almost unscathed. This result is shown in Figure 1.

If the increased supply is sustained, a periodic train of solitary waves is formed. This is best demonstrated using a syringe driver, since the rate of supply can be controlled precisely. Figure 2 shows the results of such an experiment. The response to a simple step between two uniform supply rates is a long-lived wave train. This differs from the varicose instability [Whitehead, 1982], which occurs when the Reynolds number in the interior fluid exceeds a value of about 8 [Huppert *et al.*, 1986]. In this experiment the maximum Reynolds number is about 3, and the formation of wave trains is readily observed at smaller Reynolds numbers.

Derivation of the Equations Governing Pipe Flow

The theoretical model that we have used to compare with the experiments describes the behavior of fluctuations in the diameter of a single, uniform vertical pipe in an infinite medium. We refer to the viscous wall fluid as the solid phase, and to the fluid in the pipe as the liquid. The rigorous description of this system appears to be analytically intractable, but a good approximation can be obtained as follows. Finite Reynolds number corrections are neglected in both the solid and the liquid.

The Poiseuille flow formula for the flow in the pipe, neglecting the slope of the walls, is

$$u = -\frac{\pi a^4}{8\eta^{\mathrm{liq}}}\left[\frac{\partial p^{\mathrm{liq}}}{\partial z} + \rho^{\mathrm{liq}} g\right] , \tag{1.1}$$

Text continues on page 10

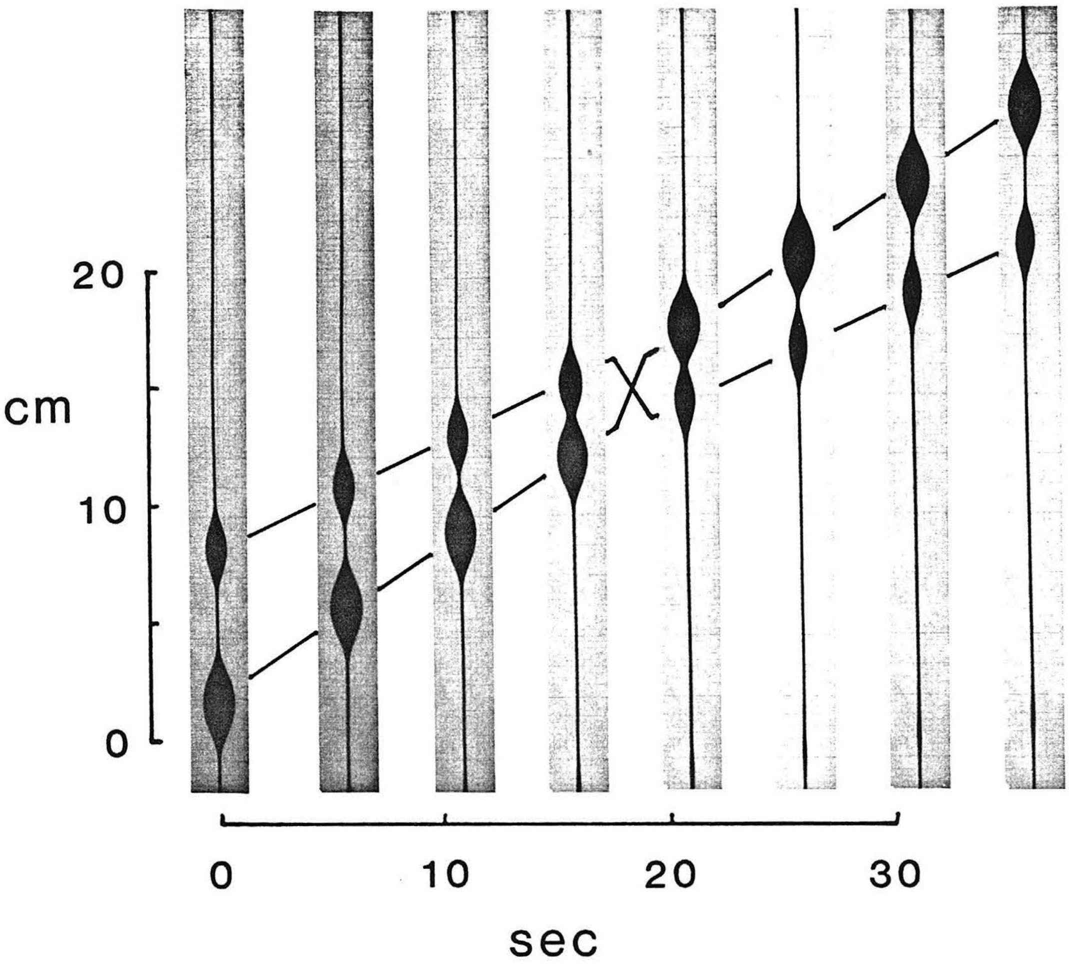

Figure 1.1. A montage showing the interaction of two solitary waves. The photographs were taken using back lighting and a flat-sided tank, to avoid distortion. Only a portion of the tank is shown in each frame; the tank is 10 cm wide. The frames are spaced according to their separation in time. In both the first three and the last three frames, the two waves ascend as solitary waves with constant amplitude, shape, and velocity. This is shown by the ruled lines. The main outcome of the interaction seen in the middle two frames is the phase shift, shown by the offset of the ruled lines. The amplitudes of the two waves are conserved very well; our measurements show that the larger waves gain a little liquid at the expense of the smaller waves. The uniform pipe is undisturbed by either the passage of the waves or the interaction.

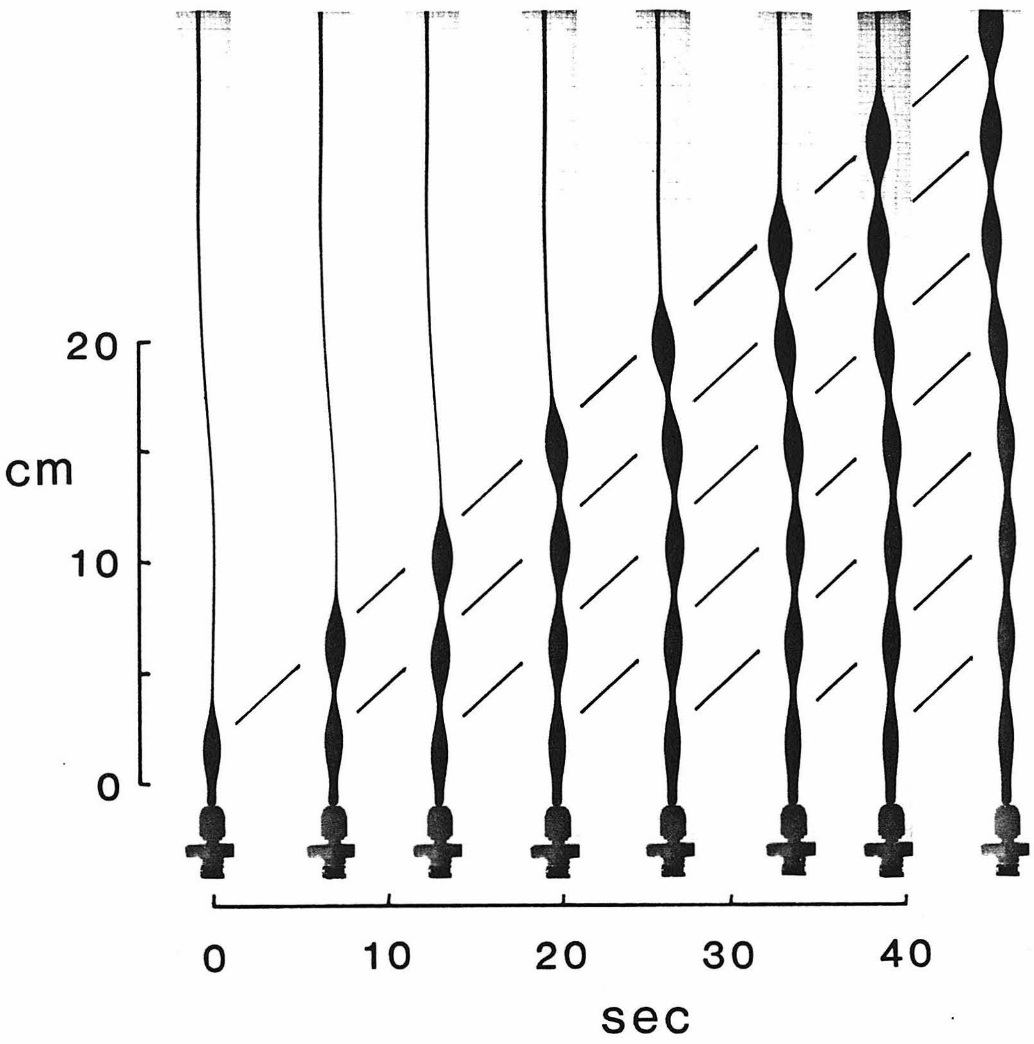

Figure 1.2. A montage showing the formation of a periodic wave train. This experiment started with a uniform pipe, sustained by a constant supply of buoyant liquid from the nozzle seen at the base of the frames. The rate of supply was then increased and held at a new constant level, approximately 220 times higher. This increase could be accommodated by the formation of a larger uniform pipe, but the system preferentially forms a periodic wave train. In longer experiments, we find that the wave train does slowly degrade down to a larger uniform pipe. The ruled lines are parallel and equally spaced.

where z is the vertical coordinate, u (z) is the volume flux of liquid through the pipe relative to the solid, a (z) is the pipe radius, ρ^{liq}, η^{liq}, and $p^{\mathrm{liq}}(z)$ are the liquid density, viscosity, and pressure, and g is the acceleration due to gravity.

The velocity and pressure fields in the solid, $\mathbf{v}^{\mathrm{sol}}$ and p^{sol}, satisfy the Stokes equation.

$$\eta^{\mathrm{sol}} \nabla^2 \mathbf{v}^{\mathrm{sol}} = \nabla p^{\mathrm{sol}} + \rho^{\mathrm{sol}} g \, \hat{\mathbf{z}} \tag{1.2}$$

The density and viscosity of the solid are ρ^{sol} and η^{sol}. Since the solid is incompressible ($\nabla . \mathbf{v}^{\mathrm{sol}} = 0$), taking the divergence of equation (1.2) shows that the pressure field satisfies Laplace's equation. If the walls of the tank are distant from the pipe, then the instantaneous pressure distribution in the solid can be represented as a sum of Fourier components of the form $p^{\mathrm{sol}}(k) = K_o(kr) \sin(kz)$, where r is the radial coordinate and k is the vertical wave number. K_o is the modified Bessel function of the second kind and zeroth order, the only solution to the radial part of the Laplacian that is bounded as $r \to \infty$. By substitution of this form into (1.2), we find that a Fourier component of the radial flow in the solid around the pipe has, in the limit $kr << 1$, the following dependence on r:

$$v_r^{\mathrm{sol}}(k) \propto \frac{1}{r} + O\left(k\, r^2 \ln(kr)\right) \ . \tag{1.3}$$

We note that we seek *a priori* solitary wave solutions with some wavelength λ. In the limit where the solid viscosity is much greater than the liquid viscosity, we find that a long wavelength approximation is justified; $2\,\pi\, a \,/\, \lambda \sim k\, a << 1$. The stress boundary condition at the pipe wall is then simple, since we need only take the 1/r term in the expansion of v_r^{sol} above. This is the same for all the Fourier components, so the Fourier sum is trivial.

We link the flow in the solid and liquid by considering the balance of forces at the pipe wall. The balance of normal stress across this boundary is approximated by

$$p^{liq} = p_0^{sol} - \rho^{sol} g z + 2 \eta^{sol} \frac{v_r^{sol}(r = a)}{a} , \tag{1.4}$$

where v_r^{sol} is now the sum of all the components of radial flow in the solid, and p_0^{sol} is the pressure at a reference level (z = 0) and at large r. We can obtain an expression for the pressure gradient driving Poiseuille flow in (1.1) by taking the derivative of (1.4) with respect to z.

$$\frac{\partial p^{liq}}{\partial z} + \rho^{liq} g = - (\rho^{sol} - \rho^{liq}) g + 2 \eta^{sol} \frac{\partial}{\partial z} \left(\frac{v_r^{sol}(r = a)}{a} \right) \tag{1.5}$$

Finally, we introduce time dependence using continuity. Clearly, $v_r^{sol}(r = a) = \partial a / \partial t$, where t is time. Also,

$$\frac{\partial u}{\partial z} = - \frac{\partial}{\partial t} (\pi a^2) . \tag{1.6}$$

Substituting (1.5) into (1.1) and using these continuity conditions, we obtain

$$u = \frac{\pi a^4}{8 \eta^{liq}} \left[g (\rho^{sol} - \rho^{liq}) + \eta^{sol} \frac{\partial}{\partial z} \left(\frac{1}{\pi a^2} \frac{\partial u}{\partial z} \right) \right] . \tag{1.7}$$

Equations (1.6) and (1.7) form a closed system in the variables a and u, which vary with z and t. They can be non-dimensionalized using the dimensional scales $L = a_0\,(\eta^{sol} / 8\,\pi\,\eta^{liq})^{1/2}$ and $T = (8\,\pi\,\eta^{sol}\,\eta^{liq})^{1/2} / a_0\,g\,(\rho^{sol} - \rho^{liq})$, where a_0 is a reference value of the pipe radius (typically that of the thin uniform pipe). Note that since $\eta^{sol} >> \eta^{liq}$, $L >> a_0$; this justifies the long wavelength approximation used earlier. In the following equations the variables with bars are non-dimensional. Specifically, $u = \overline{u} \cdot L / T$ and $a = \overline{a} \cdot a_0 / \pi^{1/2}$.

$$\frac{\partial \overline{u}}{\partial \overline{z}} = - \frac{\partial}{\partial \overline{t}} (\overline{a}^2) \tag{1.8}$$

$$\overline{u} = \overline{a}^4 \left[1 + \frac{\partial}{\partial \overline{z}} \left(\overline{a}^{-2} \frac{\partial \overline{u}}{\partial \overline{z}} \right) \right] \tag{1.9}$$

Discussion: Pipe Flow and Porous Flow

The following analogies may be drawn between this experiment and buoyancy-driven porous flow in a deformable matrix. The pipe corresponds to a permeable pathway through the matrix that the liquid can follow. The pipe radius corresponds to the porosity. The deformation of the pipe wall corresponds to the dilation or compaction of the matrix associated with changes in porosity.

As will be shown in Chapter 2, the non-dimensional Equations (1.7) and (1.8) are analogous to those governing porous flow in a deformable matrix, when the flow is constrained to one dimension (vertical). This similarity persists even if the tank walls are closer to the conduit and "plug flow" occurs in the solid, because the r^{-1} contribution to v_r^{sol} still dominates [Scott and Stevenson, 1986].

The porous flow equations are obtained by substituting the porosity $f \equiv \overline{a}^2$. The conditions of pipe flow are then shown to correspond to porous flow with an f^2 dependence for the permeability and an f^{-1} dependence for the compaction viscosity of the solid matrix. Taken literally, the equivalence above spuriously implies $f > 1$ (since we generally have $a \geq a_0$). This is physically impossible but is solely a consequence of the mathematical procedure of non-dimensionalization.

Some analysis, and numerical modeling, of solitary wave solutions to the one-dimensional porous flow equations are presented in Chapter 3. We derive explicit expressions for the dispersion relation between wave amplitude and phase velocity. For the special case of a deformable pipe, this relationship is:

$$c = \frac{a_0^2 g(\rho^{sol} - \rho^{liq})}{8\eta^l} \cdot \frac{\left[2\ln\Psi - 1 + \frac{1}{\Psi^2}\right]}{\left[1 - \frac{2}{\Psi} + \frac{1}{\Psi^2}\right]}, \tag{1.10}$$

where a_0 is the radius of the uniform part of the pipe, c is the phase velocity and $\Psi = (a_{max}/a_0)^2$. The leading quotient on the RHS is the mean Poiseuille flow velocity in the uniform pipe. Equation (1.10) demonstrates that the velocity of the waves is controlled primarily by the viscosity of the liquid.

An alternative use of the experimental apparatus is to study the ascent of the buoyant liquid in the absence of the pipe. If the pipe is absent, the analogy with porous flow breaks down. Pulses of liquid ascend as diapirs, which coalesce when they collide. The ascent velocity of the diapirs depends primarily on the viscosity of the fluid surrounding the diapir, in contrast to our statement above about the velocity of the solitary waves.

Using photographs of the experiment, we have made limited measurements of the amplitudes, ascent velocities, and wavelengths of the waves; these agree with the theory to within 10%. Waves with values of Ψ between 6 and 80 were used. Thus, we find good agreement between measurements of this experiment, measurements of the numerical experiments described in Chapter 3, and the theoretical dispersion relation. The experiments presented in the figures complement the numerical experiments presented in Chapter 3, where we similarly show a collision and the formation of a wave train. This correspondence lends credibility to the numerical studies. We note that more detailed laboratory measurements have been carried out by Olson and Christensen [1986].

Real porous media have a much more complicated microscopic structure than that discussed here. It is for this reason that the equations governing porous flow cannot be formulated with the precision of those governing pipe flow. Differing constitutive assumptions will change the functional form of the matrix permeability and viscosity, but not the existence and nature of the waves described here. More importantly, real porous media are three-dimensional; numerical experiments presented in Chapter 4 indicate that the one-dimensional waves are unstable in higher dimensions, but that solitary waves of higher dimensions are formed. The balance of dissipative mechanisms and gravitational energy release governing the ascent of these waves is the same in one, two, or three dimensions. We believe, therefore, that the experiments described here not only are pedagogically useful, but also serve as a laboratory analogue for real earth processes. Specifically, we may expect the geochemistry, morphology, and timing of igneous processes to be affected by phenomena resembling those reported here: this is discussed in Chapter 3. It is also possible that solitary waves arise in other porous systems.

In stressing the role of pipe flow experiments as analogues of porous flow, we overlook a more direct application. In mantle convection, material that is hot, but not molten, is still more buoyant and less viscous than its surroundings. It may be that the temperature dependence of viscosity leads to a pattern of convection in which upgoing material ascends as waves on preheated "pipes." The characteristic of these waves in leaving the pipe undisturbed may account for the fixity of mantle plumes. Olson *et al.* [1986] claim to have observed pipe waves in numerical simulations of convection with temperature-dependent viscosity, and argue that they have the correct periodicity to account for the episodicity of volcanism in the Hawaiian island chain.

CHAPTER 2

A MATHEMATICAL MODEL OF POROUS FLOW AND VISCOUS COMPACTION

Abstract

A simple model of a permeable partially molten rock is justified on the basis of experimental observations. The microscopic processes of porous flow and compaction are discussed and related to macroscopic constitutive assumptions. A mathematical description of the system is developed, based on Darcy's law and a constitutive equation for the viscous matrix. In this development, we stress the parallels between porous flow and pipe flow, and the qualitative differences between porous flow and circulation. The governing equations are non-dimensionalized and alternative derivations are discussed.

Introduction

The missing element in a physical model of the buoyant ascent of a liquid by porous flow has been a description of the deformation and compaction of the matrix. This is necessary because the liquid cannot escape from a closed porous system unless the matrix compacts to fill the space it leaves. This process has been discussed in the past [Sleep, 1974; Stolper *et al.*, 1981; Turcotte and

Ahern, 1978]; a full mathematical description has been supplied recently by several authors [Scott and Stevenson, 1984 and 1986; Stevenson and Scott, 1987; McKenzie, 1984; Fowler, 1985]. In particular, a definitive introduction has been provided by McKenzie [1984]. All of these mathematical models start with the essentially the same model physical system. Acknowledging some differences in the mathematical assumptions, they all end up with mathematically equivalent governing equations. Some insight can be gained by examining the different paths taken between these end-points; this is the focus of the discussion at the end of the chapter. The derivation presented below is an augmented version of that presented by Stevenson and Scott [1987].

There are two substantive differences between the pipe flow analogue described in Chapter 1 and even the simplest description of a permeable partial melt. First, a porous medium is three-dimensional. Whereas the pipe radius varies only with vertical position, the porosity can vary both vertically and laterally. As a consequence the governing equations have a more complicated appearance, but also the physical process of circulation is allowed, which has no analogue in the pipe flow. This difference will be clarified when the equations are obtained. Secondly, the microscopic complexity of a porous medium prevents us from treating the flow in every pore and every grain precisely. Whereas in pipe flow we can calculate the flow at every point in the system, we must treat the flow fields as quantities averaged over many grains. This leads to a need for macroscopic constitutive assumptions: we acknowledge that information is lost this way and must hope that the assumptions are consistent with the true microscopic behavior. The credibility of our large-scale description is based primarily upon a qualitative understanding of the microscopic appearance of the system. This will be discussed below before the mathematical model is developed.

Partially Molten Rocks

Microscopic Texture. Our confidence in macroscopic fluid-dynamical modeling is based on a single microscopic property of partially molten rocks. This is the control that surface energies exert on the local configuration of the two phases. Observations of partially molten rocks of ultramafic [Waff and Bulau, 1979; Cooper and Kohlstedt, 1986; Vaughan *et al.*,, 1982] and felsic [Jurewicz and Watson, 1985] composition are consistent with a theoretical model in which the geometry of the liquid phase adjusts to minimize the local surface energy. The system minimizes the sum of the surface areas of liquid-solid interfaces (pore walls) and solid-solid interfaces (grain boundaries), multiplied by their respective surface energies. Calculations based on this principle [von Bargen and Waff, 1986] show that the theory is consistent with the observations.

Figure 2.1 shows a schematic example of the equilibrium geometry to which a partial melt evolves. The precise configuration of the two phases depends on the relative magnitude of the surface energies, parameterized by the dihedral angle (see the caption to Figure 2.1). This is discussed in the metallurgical literature by, e.g., Beeré [1975], as well as in the references mentioned above. The important conclusion for our purposes is that, for dihedral angles less than 60°, the liquid remains interconnected down to infinitesimal porosities. For larger dihedral angles, some finite porosity must be reached before a stable interconnected network is formed. Despite some difficulties in correctly measuring the dihedral angle [Jurewicz and Jurewicz, 1986], all observations of olivine-basalt assemblages display dihedral angles significantly less than 60°. Porous flow of the liquid through the solid matrix is therefore possible at low porosities. Observations of felsic systems suggest that the dihedral angle may exceed 60°, so that porous flow may be prevented at low porosities. There are other reasons for believing that porous flow and compaction are not important mechanisms in

Text continues on page 20

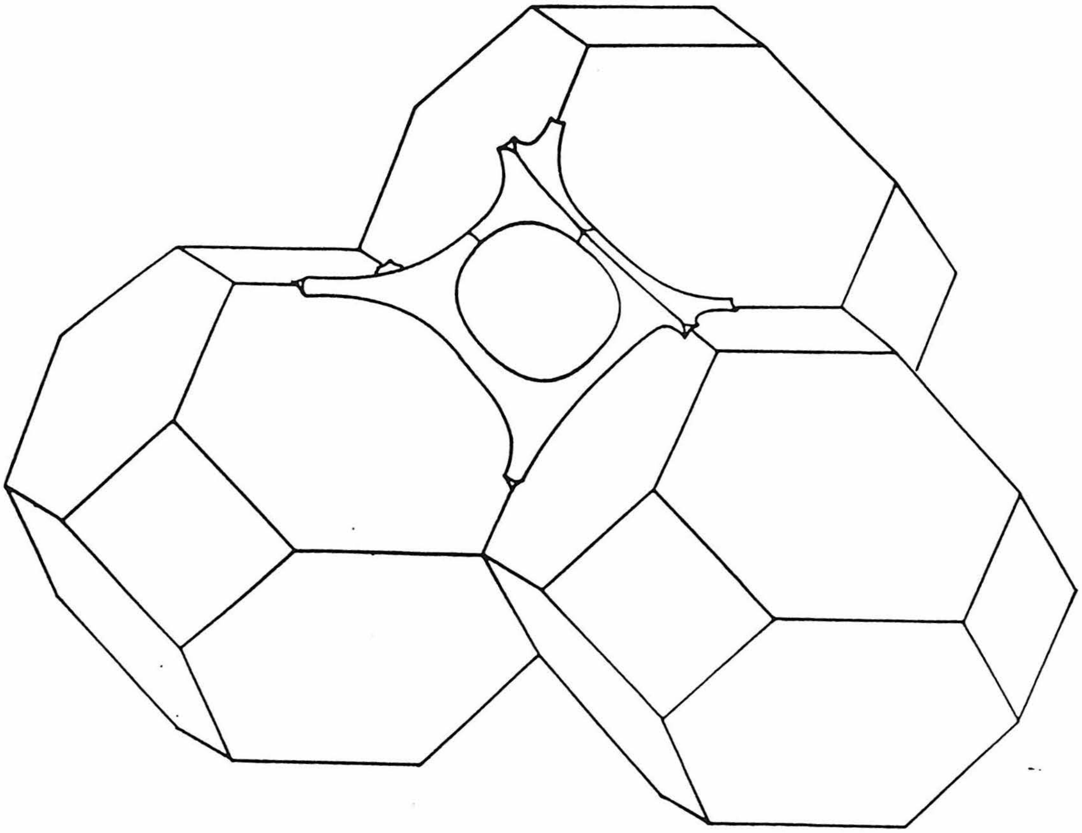

Figure 2.1. The microscopic texture of an idealized partially molten rock. The liquid lies primarily in tubules along the three-grain edges, forming an interconnected network in three dimensions. The triangular cross section of the tubules has been observed repeatedly in ultramafic assemblages. The interior angle at the corners of this cross section is the dihedral angle between the two phases. Figure taken from von Bargen and Waff [1986].

the segregation of granites; see Wickham [1987] for a comprehensive review of this subject.

Returning to ultramafic rocks, we conclude that microscopic equilibration based on the reduction of surface energy provides us with a well-behaved system that, with some confidence, we can describe by macroscopic properties. The surface forces that we value so much at the microscopic level can also have macroscopic dynamic effects. This issue was first raised by Waff [1980]. A mathematical model for this process has now been provided by Stevenson [1986], who concludes that it is unlikely that surface forces have important macroscopic effects in ultramafic partial melts. They may be important in the migration of water-rich fluids because of their low viscosity.

In order to construct a macroscopic fluid-dynamical description of this system, we must consider the rheology and the permeability of the matrix. These are discussed below.

Rheological Description of the Matrix. The novel feature of this physical model is the dynamic deformation of the matrix. It is therefore natural to start by considering the rheological description of the matrix. Take an isotropic and locally uniform element of the matrix, large compared to the grain size but small compared to the scale length of variations in quantities such as the porosity and grain size. The rheological behavior of this element can be divided into two types of flow.

The first is simple shear, with no compaction occurring, described by the constitutive relation:

$$(1 - f)\,\sigma'_{ij} = \eta\,(f)\,\dot{e}_{ij} \qquad (i \neq j)\,, \tag{2.1}$$

where σ'_{ij} is the deviatoric stress in the solid. The strain rate $\dot{e}_{ij}$ is defined in terms of gradients of the velocity of the solid matrix, in the usual way. The shear stress is related to the shear strain rate by a viscosity η, which can be a function of porosity. Specifically, η is expected to decrease as the porosity increases. This decrease may be due in part to the reduction of material in the matrix framework and in part to liquid-enhanced creep processes. The factor $(1 - f)$ appears because the stress is defined continuously, but acts only on the solid part of an element of area in the two-phase medium.

The second type of flow is pure compaction. The porosity is reduced, and liquid is expelled due to a different state of stress in the matrix and the liquid. We define a bulk viscosity ς, relating the rate of compaction to the pressure difference between the two phases.

$$(1 - f)\,(p^{liq} - p^{sol}) = \varsigma(f)\,\dot{e}_{kk} \tag{2.2}$$

We note that it is different from the bulk viscosity of a single compressible phase, although it is mathematically similar. The flow associated with this viscosity is occurring on the scale of the grain size. This microscopic flow could involve whole grain deformation, grain boundary diffusion, and liquid-enhanced processes around the pore space. In (2.2) we ignore the difference in pressure between the phases due to surface tension. This approximation can arguably be justified because surface tension is a conservative force; for a full discussion see Stevenson [1986].

The constitutive forms above can be combined in a single constitutive relation:

$$\begin{aligned}(1 - f)\,(\sigma'_{ij} + (p^{liq} - p^{sol})\,\delta_{ij}) &= \\ (1 - f)\,(\sigma^{sol}_{ij} + p^{liq}\,\delta_{ij}) &= (\varsigma - {}^{2}\!/_{3}\eta)\,\dot{e}_{kk}\,\delta_{ij} + 2\,\eta\,\dot{e}_{ij}\,.\end{aligned} \tag{2.3}$$

The constitutive relation is like that used for a compressible fluid, except that the liquid pressure appears as a reference for the pressure in the solid matrix. Compaction should not occur when these are equal.

We know of two experimental studies that provide estimates of the rheological parameters η and ς. The first is that of Cooper and Kohlstedt [1984]. The purpose of these experiments was to investigate the importance of liquid-enhanced processes in the compaction of an olivine aggregate; the liquid used was a synthetic silicate of basaltic composition. The compaction process differed from that defining ς because it occurred through the collapse of void space, not through the expulsion of liquid. However, the results are important because they demonstrate that the rate-limiting process in the compaction is transport along solid-solid grain boundaries, where the liquid is absent. There is a modest increase in the rate of compaction when liquid is present because the diffusion path in the grain boundaries is shortened by the presence of liquid in the pores. The grain size used in these experiments was around 10 μm, so we must extrapolate to obtain a value of the bulk viscosity applicable to coarse-grained mantle rocks. McKenzie [1985] obtains a value of 3×10^{18} Pa s for 1 mm grains, at a temperature of 1300° C and 15% porosity.

The second study is that of Auer *et al.* [1981], in which they subjected partially molten fine-grained granite to moderate deviatoric stresses, under conditions of much greater hydrostatic stress. They also concluded that the creep rate was limited by solid-state processes, up to a critical value of around 20% liquid. At this point the shear viscosity drops due to loss of structural integrity of the matrix, as proposed by Arzi [1978]. In light of these studies, we propose values for η and ς equal to the likely shear viscosity of crystalline mantle material close to the solidus, perhaps 10^{19} Pa s, reflecting a small degree of liquid-enhancement.

Permeability of the Matrix. A second material property, the permeability of a partially molten rock, is also unknown. The functional dependence of the permeability k on the porosity f has a major impact on quantitative aspects of porous flow phenomena. To condense various arguments, consider a simple form for the permeability:

$$k = \frac{a^2 f^n}{b} , \tag{2.4}$$

where a is the grain size and n and b are dimensionless parameters. The notation is that used by Richter and McKenzie [1984].

We feel that there is theoretical and experimental justification for a value of n between 2 and 3 for partially molten rocks of low ($<$20%) porosity. The Blake-Kozeny-Carman equation is widely used to model the permeabilities of porous systems. The theoretical basis of this equation, described by Carman [1937], dictates that the exponent n is determined by the functional dependence of the mean hydraulic radius on porosity. The mean hydraulic radius is the reciprocal of the surface area of the pore space per unit volume; it is therefore an inverse measure of the resistance of the network to flow. This assumption leads to $n = 2$ for a network of randomly oriented tubes of constant cross section and to $n = 3$ for a bed of packed spheres. (Strictly, k varies as $f^3 / (1 - f)^2$ in this case; the denominator has negligible effect when $f << 1$). The texture of partially molten ultramafic rocks lies, subjectively, between these two cases. The experiments of Maaløe and Scheie [1982] support this qualitative argument. They determined the rate of flow of liquids through a model porous system of compacted glass beads, intended to imitate the texture of partially molten rock. For porosities in the range between 0.5% and 20%, the data are fit best by a value of n between 2 and 3.

The value of the multiplicative constant b is less critical. Its value is partly determined by the tortuosity of the network, expressed by the ratio of the distance between two points in the system and the actual distance traveled by the liquid between those points. Suggested values for this and the remaining material properties of importance are tabulated in Chapter 3.

As noted by McKenzie [1984], it is likely that the porous network remains interconnected down to very small porosities, at least for the olivine-basalt systems that have been studied experimentally. This is due to the control of surface energies on the microscopic texture of the partial melt. Toramaru and Fujii [1986] have suggested that the presence of orthopyroxenes in the mineral assemblage leads to non-connectivity of the porous network. This may call for some adaptation of the permeability function used in modeling.

Derivation of the Governing Equations

General description of the model system. We think of the partially molten system as a spongelike crystalline matrix saturated with liquid. The porosity of the matrix phase and the volume fraction of liquid are therefore synonymous. Both the matrix material and the liquid are assumed to be fully connected. Both phases are considered to be incompressible. We use averaged values of the variables such as porosity, velocity, and stress. This averaging is performed on a scale much larger than the grain size but much smaller than the scale of compaction processes. We also assume that the Reynolds number is small for the flow of both phases, so that all inertial terms may be neglected.

Choice of velocity variables. The frame of reference that we use for the two-phase system must be considered carefully. In connection with this, it proves useful to define the center-of-mass velocity $\mathbf{V}^{com}$ for any two-phase element as follows:

$$\mathbf{V}^{\mathrm{com}} = \mathrm{f}\,\mathbf{V}^{\mathrm{liq}} + (1-\mathrm{f})\,\mathbf{V}^{\mathrm{sol}}\,. \tag{2.5}$$

This velocity field does not describe the motion of any actual particle of solid or liquid. However, since we assume that both phases are incompressible, $\mathbf{V}^{\mathrm{com}}$ has the useful property of being divergence-free. Hereafter we will refer to this velocity field as the **circulation** for this reason.

The solid, the liquid, and the center-of-mass of an element all move relative to a global frame of reference fixed in space, although it is clear from (2.5) that only two of the three velocity fields are independent. We would therefore prefer to use only two of the three in writing down the governing equations. $\mathbf{V}^{\mathrm{com}}$ is a good choice for one of the independent fields; it describes the average motion of the two phases while making no statement about the relative motion of porous flow. By preventing circulation through the perimeter of a region we automatically conserve mass. We use a perimeter with this property as a fixed global frame of reference. The second field can now be chosen as the velocity of one of the phases relative to the local center-of-mass velocity. This places us in a local frame and allows us to view the porous flow without concern for the motion of the local frame relative to the fixed global frame. We prefer to use $\mathbf{V}^{\mathrm{sol}} - \mathbf{V}^{\mathrm{com}}$ because $\mathbf{V}^{\mathrm{sol}}$ appears in the constitutive relation for the solid. Hereafter we refer to $\mathbf{V}^{\mathrm{sol}} - \mathbf{V}^{\mathrm{com}}$ as the **porous flow.** At any time the liquid velocity (probably the quantity of most interest) can be recovered from the porous flow and circulation, using (2.5).

Equations governing the flow fields. We now move into the local frame of reference of a two-phase element and make statements about the flow in the solid and liquid, just as we did for the pipe flow in Chapter 1. Replacing Poiseuille flow in the pipe, we have Darcy's law:

$$V_i^{sol} - V_i^{com} = - f\,(V_i^{liq} - V_i^{sol}) = \frac{k}{\eta^{liq}} \left[\frac{\partial p^{liq}}{\partial x_i} + g\,\rho^{liq}\,\delta_{iz} \right] , \qquad (2.6)$$

where ρ^{liq}, and η^{liq} are the liquid density and viscosity. This "law" is actually an empirical statement that defines the permeability k as the constant of proportionality between the flux of liquid relative to the solid, and the pressure gradient in the liquid relative to the hydrostatic gradient. As discussed above, k has a strong dependence on the porosity f. The original experimental form of Darcy's law naturally involves $\mathbf{V}^{liq} - \mathbf{V}^{sol}$; in (2.6) it is recast in terms of the porous flow field $\mathbf{V}^{sol} - \mathbf{V}^{com}$, using (2.5).

The effect of the flow in the solid is described by the constitutive relation (2.3) discussed above. Writing out the strain rates in (2.3) explicitly,

$$(1 - f)\,(\sigma_{ij} + p^{liq}\,\delta_{ij}) = (\varsigma - {}^{2}\!/_{3}\eta)\,\frac{\partial V_k^{sol}}{\partial x_k}\,\delta_{ij} + \eta \left\{ \frac{\partial V_i^{sol}}{\partial x_j} + \frac{\partial V_j^{sol}}{\partial x_i} \right\} . \qquad (2.7)$$

As mentioned above, $\mathbf{V}^{sol}$ is used as a primary variable because of its explicit appearance in this expression.

For the pipe flow, the flow in the solid and liquid were linked using a force balance boundary condition at the pipe wall. Here we use force balance on a two-phase element for the same purpose, equating the forces acting on the solid and liquid parts of the surface to the body forces within the element.

$$\int_{\mathrm{sol}} \sigma_{ij}^{\mathrm{sol}}\, dS_j - \int_{\mathrm{liq}} p^{\mathrm{liq}}\, \delta_{ij}\, dS_j = \int_{\mathrm{sol+liq}} \Big((1-f)\, \sigma_{ij}^{\mathrm{sol}} - f\, p^{\mathrm{liq}}\, \delta_{ij}\Big)\, dS_j \qquad (2.8a)$$

$$= \int_{\mathrm{sol+liq}} g\Big((1-f)\, \rho^{\mathrm{sol}} + f\, \rho^{\mathrm{liq}}\Big)\, \delta_{iz}\, dV$$

We have assumed that the volume porosity f is equal to the "surface porosity," i.e., the fraction of an arbitrary surface that lies in the liquid phase. By the divergence theorem,

$$\frac{\partial}{\partial x_j}\Big((1-f)\, \sigma_{ij}^{\mathrm{sol}} - f\, p^{\mathrm{liq}}\, \delta_{ij}\Big) = g\Big((1-f)\, \rho^{\mathrm{sol}} + f\, \rho^{\mathrm{liq}}\Big)\ \delta_{iz}\, . \qquad (2.8b)$$

Equations (2.6), (2.7), and (2.8b) can be manipulated into a more useful form as follows. Rearranging (2.8b) leads to an expression for the pressure gradient in Darcy's law (2.6).

$$\frac{\partial p^{\mathrm{liq}}}{\partial x_i} + g\, \rho^{\mathrm{liq}}\, \delta_{iz} = \frac{\partial}{\partial x_j}\Big((1-f)(\sigma_{ij}^{\mathrm{sol}} + p^{\mathrm{liq}}\, \delta_{ij})\Big) - (1-f)\, g\, \Delta\rho\, \delta_{iz}\, , \qquad (2.9)$$

where $\Delta\rho = \rho^{\mathrm{sol}} - \rho^{\mathrm{liq}}$. Substituting this into (2.6),

$$V_i^{\mathrm{sol}} - V_i^{\mathrm{com}} = \frac{k}{\eta^{\mathrm{liq}}}\left[-(1-f)\, g\, \Delta\rho\, \delta_{iz} + \frac{\partial}{\partial x_j}\Big((1-f)\, (\sigma_{ij}^{\mathrm{sol}} + p^{\mathrm{liq}}\, \delta_{ij})\Big)\right]. \qquad (2.10)$$

Substituting from the constitutive relation (2.7) into (2.10),

$$V_i^{sol} - V_i^{com} = \frac{k}{\eta^{liq}} \Bigg[- (1-f)\, g\, \Delta\rho\, \delta_{iz} + \frac{\partial}{\partial x_j} \left\{ (\varsigma - {}^2\!/_3\eta) \frac{\partial V_k^{sol}}{\partial x_k} \delta_{ij} + \eta \left\{ \frac{\partial V_i^{sol}}{\partial x_j} + \frac{\partial V_j^{sol}}{\partial x_i} \right\} \right\} \Bigg] . \quad (2.11)$$

This equation is readily interpreted. The relative motion of porous flow, on the LHS, is driven by the density difference but modified by a term that depends on the velocity gradients in the solid associated with compaction and shear. In their absence the familiar algebraic form of Darcy's law is recovered. The permeability conceals a strong non-linearity arising through its dependence on f. $\mathbf{V}^{com}$ occurs only as a background velocity field upon which $\mathbf{V}^{sol}$ is superimposed.

In Chapter 4 two sets of calculations are presented, The first uses an approximation in which $\mathbf{V}^{com}$ is omitted from (2.10), effectively removing one of the two independent velocity fields. For the second set, this approximation is removed, so that we must obtain an independent equation to solve for $\mathbf{V}^{com}$. Remembering that $\nabla . \mathbf{V}^{com} = 0$, we complicate the constitutive relation (2.7) by adding and subtracting terms in $\mathbf{V}^{com}$.

$$(1-f)(\sigma_{ij} + p^{liq}\,\delta_{ij}) = \eta \left\{ \frac{\partial V_i^{com}}{\partial x_j} + \frac{\partial V_j^{com}}{\partial x_i} \right\} + (\varsigma - {}^2\!/_3\eta) \frac{\partial\,(V_k^{sol} - V_k^{com})}{\partial x_k}\, \delta_{ij} + \eta \left\{ \frac{\partial\,(V_i^{sol} - V_i^{com})}{\partial x_j} + \frac{\partial\,(V_j^{sol} - V_j^{com})}{\partial x_i} \right\} \quad (2.12)$$

The reason for this maneuvering is to express the stress in the solid in terms of $\mathbf{V}^{com}$, with a correction term that depends on $\mathbf{V}^{sol} - \mathbf{V}^{com}$. Substituting (2.12) into (2.9)

$$\eta \frac{\partial^2 V_i^{com}}{\partial x_j^2} - \frac{\partial p^{liq}}{\partial x_i} = g\ (\rho^{sol} - f\ \Delta\rho)\ \delta_{iz} - A_i\ , \tag{2.13}$$

where

$$A_i = \frac{\partial}{\partial x_j} \left[(\varsigma - {}^2/_3\eta)\ \frac{\partial\ (V_k^{sol} - V_k^{com})}{\partial x_k}\ \delta_{ij} \right.$$

$$\left. + \eta \left\{ \frac{\partial\ (V_i^{sol} - V_i^{com})}{\partial x_j} + \frac{\partial\ (V_j^{sol} - V_j^{com})}{\partial x_i} \right\} \right] . \tag{2.14}$$

Equation (2.13) may be written in vector notation,

$$\eta \nabla^2 \mathbf{V}^{com} - \nabla p^* = -\ f\ g\ \Delta\rho\ \hat{\mathbf{z}} - \mathbf{A}\ . \tag{2.15}$$

Equation (2.15) shows that the circulation is governed by a modified form of the familiar Stokes equation for creeping flow of a viscous fluid. Viscous stresses and pressure gradients, on the LHS, are balanced by body forces on the RHS. The pressure variable p^* in (2.15) is the liquid pressure relative to the lithostatic gradient, i.e., $p^* = p^{liq} + g\ \rho^{sol}\ z$. The first term on the RHS is buoyancy force due to variations in porosity; more porous regions are buoyant because they contain more liquid. The second term on the RHS, $\mathbf{A}$, is not a body force but the correction to the viscous stresses because it is $\mathbf{V}^{sol}$, not $\mathbf{V}^{com}$, that appears in the original constitutive relation. It is sometimes useful, however, to think of $\mathbf{A}$ as a body force arising because porous flow and compaction is occurring. In (2.14) $\mathbf{A}$ depends only on gradients of $\mathbf{V}^{sol} - \mathbf{V}^{com}$; it vanishes if porous flow is not permitted or is uniform. Note also that the permeability does not appear explicitly in Equation (2.15).

Equation (2.11) for the porous flow and Equation (2.15) for the circulation describe all the dynamics of the two-phase system and show clearly how the two types of flow interact. This interaction will investigated further in the latter part of Chapter 4.

Time dependence. So far we have derived equations that fully define a boundary value problem in space, but with no mention of the evolution of the system through time. As in pipe flow, time is introduced by requiring continuity of the two-phase system, which allows us to relate the rate of compaction to the flow fields.

$$\frac{\partial f}{\partial t} = (1 - f)\, \nabla.\mathbf{V}^{sol} - \mathbf{V}^{sol}.\nabla\, f\, . \tag{2.16}$$

The porosity within a two-phase element fixed in space changes in response to two effects. On the RHS, the first term is the rate at which solid material is leaving the element. The factor of (1 – f) multiplies the divergence of the solid velocity because the solid occupies this fraction of the surface of the element. The second term describes the advection of porosity: in a region with a porosity gradient, flow of the solid matrix will bring material with a different porosity into the element. Some additional insight may be gained by rewriting (2.16) in terms of both $\mathbf{V}^{sol}$ and $\mathbf{V}^{com}$.

$$\frac{\partial f}{\partial t} = \nabla.\left\{(1 - f)\,(\mathbf{V}^{sol}-\mathbf{V}^{com})\right\} - \mathbf{V}^{com}.\nabla\, f \tag{2.17}$$

This statement is permitted because $\nabla.\mathbf{V}^{com} = 0$. The change of porosity is now divided clearly into a compaction term due to the porous flow and an advection term due to the circulation.

We can now bring together a complete system of equations in the vector variables $\mathbf{V}^{sol}$ and $\mathbf{V}^{com}$ and the scalar variables f and p*, a total of eight unknowns in three-dimensional space.

- Matrix Permeability

$$k = \frac{a^2 f^n}{b} \tag{2.4}$$

- Matrix Rheology

$$(1 - f)\,(\sigma_{ij} + p^{liq}\,\delta_{ij)} = (\varsigma - {}^2\!/_3\eta)\,\frac{\partial V_k^{sol}}{\partial x_k}\,\delta_{ij} + \eta\left\{\frac{\partial V_i^{sol}}{\partial x_j} + \frac{\partial V_j^{sol}}{\partial x_i}\right\} \tag{2.7}$$

- Darcy's Law

$$V_i^{sol} - V_i^{com} = \frac{k}{\eta^{liq}}\left[-\,(1 - f)\,g\,\Delta\rho\,\delta_{iz} + \frac{\partial}{\partial x_j}\Big((1 - f)\,(\sigma_{ij}^{sol} + p^{liq}\,\delta_{ij})\Big)\right] \tag{2.10}$$

- Stokes Equation

$$\eta\nabla^2\mathbf{V}^{com} - \nabla p^* = -\,f\,g\,\Delta\rho\,\hat{\mathbf{z}} - \mathbf{A} \tag{2.15}$$

- "Body Force"

$$\begin{aligned} A_i = \frac{\partial}{\partial x_j}\Bigg((\varsigma - {}^2\!/_3\eta)\,&\frac{\partial\,(V_k^{sol} - V_k^{com})}{\partial x_k}\,\delta_{ij} \\ &+ \eta\left\{\frac{\partial\,(V_i^{sol} - V_i^{com})}{\partial x_j} + \frac{\partial\,(V_j^{sol} - V_j^{com})}{\partial x_i}\right\}\Bigg) \end{aligned} \tag{2.14}$$

- Compaction

$$\frac{\partial f}{\partial t} = (1 - f)\, \nabla.\mathbf{V}^{sol} - \mathbf{V}^{sol}.\nabla\, f \tag{2.16}$$

- Continuity

$$\nabla.\mathbf{V}^{com} = 0 \tag{2.18}$$

The variable p^{liq} appears above but is eliminated when the constitutive form (2.7) is substituted into Darcy's law (2.10). The eight equations needed to constrain eight unknowns are represented by Darcy's law (2.10), the Stokes equation (2.15), and the equations for compaction (2.16) and continuity (2.18).

Non-Dimensionalization. While the above set of equations have clear connections to the physical system under study, they are distinctly cumbersome. We can improve matters, and gain some additional physical insight, by non-dimensionalizing the system. To guide our choice of dimensional scales we simplify Darcy's law (2.11) by confining all the motions and their derivatives to the vertical direction and omitting the circulation.

$$V_z^{sol} = \frac{a^2\, f^{\,n}}{b\eta^{liq}} \left[- (1 - f)\, g\, \Delta\rho + \frac{\partial}{\partial z} \left\{ (\varsigma + {}^4\!/_3\eta)\, \frac{\partial V_z^{sol}}{\partial z} \right\} \right] \tag{2.19}$$

We refer to the combination $\varsigma + {}^4\!/_3\eta$ as the compaction viscosity of the matrix. It governs the behavior of the system under one-dimensional compaction. The form of (2.19) immediately suggests the use of a velocity scale V given by

$$V = \frac{a^2\, g\, \Delta\rho}{b\, \eta^{liq}}\ . \tag{2.20}$$

Replacing V_z^{sol} in (2.19) with $\overline{V} = V_z^{sol} / V$,

$$\overline{V} = f^n \left[- (1 - f) + \frac{a^2}{b\ \eta^{liq}} \frac{\partial}{\partial z} \left\{ (\varsigma + {}^4/_3\eta) \frac{\partial \overline{V}}{\partial z^2} \right\} \right] . \qquad (2.21)$$

To remove the remaining dimensional quantities from (2.21) we set $\overline{z} = z / L$, where the length scale L is given by

$$L = a \left\{ \frac{(\varsigma + {}^4/_3\eta)}{b\ \eta^{liq}} \right\}^{1/2} . \qquad (2.22)$$

V and L define a time scale T given by

$$T = L / V = \frac{\left\{ (\varsigma + {}^4/_3\eta)\ b\ \eta^{liq} \right\}^{1/2}}{g\ \Delta\rho\ a} . \qquad (2.23)$$

The values of these scales in the earth determine when and where compaction processes will be important; this matter will be discussed in Chapter 3. For the present, note that the length scale L depends on the ratio of the compaction viscosity of the solid and the liquid viscosity. Since this ratio is so large, it is possible for L to be large enough to have geological importance, despite the smallness of the grain size a.

The complete set of equations presented above can now be non-dimensionalized using V, L, and T. At this point we also shift to the explicit use of velocity components instead of suffix notation, and into two-dimensional Cartesian coordinates (z, x). In these coordinates the components of $\mathbf{V}^{sol}$ are (w, u), and the components of $\mathbf{V}^{com}$ are (W, U). Partial differentiation with respect to z, x, and t is indicated by suffixes.

- Darcy's Law

$$w - W = f^{n} \left[-(1-f) + w_{zz} + \alpha\, w_{xx} + (1-\alpha)\, u_{xz} \right] \tag{2.24a}$$

$$u - U = f^{n} \left[u_{xx} + \alpha\, u_{zz} + (1-\alpha)\, w_{xz} \right] \tag{2.24b}$$

- Stokes Equation

$$\alpha(W_{zz} + W_{xx}) - p_z^{*} = \tag{2.25a}$$

$$- f - \left[(w-W)_{zz} + \alpha\, (w-W)_{xx} + (1-\alpha)\, (u-U)_{xz} \right]$$

$$\alpha(U_{zz} + U_{xx}) - p_x^{*} = - \left[(u-U)_{xx} + \alpha\, (u-U)_{zz} + (1-\alpha)\, (w-W)_{xz} \right] \tag{2.25b}$$

- Continuity

$$W_z + U_x = 0 \tag{2.26}$$

- Compaction

$$f_t = (1-f)\,(w_z + u_x) - (w\, f_z + u\, f_x) \tag{2.27}$$

The only independent quantity that has survived our non-dimensionalization is the ratio α of the shear viscosity of the solid to the compaction viscosity.

$$\alpha = \frac{\eta}{(\varsigma + {}^{4}/_{3}\eta)} \tag{2.28}$$

As the ratio of the shear and bulk viscosities varies, $0 < \alpha < {}^3/_4$. It is clear that the compaction processes in (2.24a,b) are governed by combinations of the shear and compaction viscosity. The appearance of α alone on the LHS of (2.25a,b) shows that the circulation is primarily controlled by the shear viscosity. The variation of the behavior of the system with changing α will be discussed in Chapter 4.

In presenting the above system of non-dimensional equations we have assumed that the solid viscosities are constant. Since they appear inside a derivative in (2.19), for example, we should investigate the consequences of allowing a substantial variation of viscosity with porosity. This analysis also allows us to make a precise connection with the equations derived for pipe flow in Chapter 1. Let the compaction viscosity in (2.19) take the form $\eta_0 \, f^{-m}$. If we then use η_0 in the expressions for L, V, and T, the non-dimensional form of (2.19) is:

$$\overline{V} = f^{n} \left[-1 + \frac{\partial}{\partial \overline{z}} \left(f^{-m} \frac{\partial \overline{V}}{\partial \overline{z}} \right) \right] . \tag{2.29}$$

A factor of (1 – f) has been replaced by unity on the RHS. This is acceptable in one dimension, as the variation can be absorbed into the constitutive forms. It is not acceptable in the full, multi-dimensional form of the equations with circulation. If the factor on the RHS of Darcy's law in (2.24a), for example, is set to unity, we should also omit the buoyancy force on the RHS of the Stokes equation (2.25a). This is a physically important term, particularly in the limit where circulation is permitted but porous flow is not. This a subtle point whose significance will be clarified in Chapter 4.

The one-dimensional form of the continuity equation (2.16) is

$$\frac{\partial \overline{V}}{\partial \overline{z}} = \frac{\partial f}{\partial \overline{t}} \, . \tag{2.30}$$

Direct comparison of (2.29) and (2.30) with (1.7) and (1.8) confirms that a close analogy exists between pipe flow and porous flow, an assertion first made in Chapter 1. Our use of the liquid flux, in Chapter 1, instead of the solid velocity, here, changes the sign of $\overline{V}$. With appropriate choices for n and m, the two pairs of equations are then identical. Note that we are at liberty to choose any reasonable values for n and m since they are part of our constitutive assumptions for the permeability and rheology, respectively.

For completeness, we present the form of Darcy's law (2.24a,b) and the Stokes equation (2.25a,b) in axisymmetric cylindrical coordinates (z, r), because the translation of the stresses from Cartesian coordinates is not straightforward. The components of the solid velocity and the circulation are now (w, υ) and (W, Υ), respectively.

- Darcy's Law

$$w - W = f^{\,n} \left[-(1-f) + w_{zz} + \alpha \left(w_{rr} + \frac{w_r}{r} \right) + (1-\alpha) \left(\upsilon_{rz} + \frac{\upsilon_z}{r} \right) \right] \tag{2.31a}$$

$$\upsilon - \Upsilon = f^{\,n} \left[\upsilon_{rr} + \frac{\upsilon_r}{r} - \frac{\upsilon}{r^2} + \alpha\, \upsilon_{zz} + (1-\alpha)\, w_{rz} \right] \tag{2.31b}$$

- Stokes Equation

$$\alpha\left(W_{zz} + W_{rr} + \frac{W_r}{r}\right) - p_z^* = -f - \left[(w-W)_{zz}\right. \tag{2.32a}$$

$$\left. + \alpha\left((w-W)_{rr} + \frac{(w-W)_r}{r}\right) + (1-\alpha)\left((\upsilon-\Upsilon)_{rz} + \frac{(\upsilon-\Upsilon)_z}{r}\right)\right]$$

$$\alpha\left(\Upsilon_{zz} + \Upsilon_{rr} + \frac{\Upsilon_r}{r}\right) - p_r^* = -\left[(\upsilon-\Upsilon)_{rr} + \frac{(\upsilon-\Upsilon)_r}{r} - \frac{(\upsilon-\Upsilon)}{r^2}\right. \tag{2.32b}$$

$$\left. + \alpha\,(\upsilon-\Upsilon)_{zz} + (1-\alpha)\,(w-W)_{rz}\right]$$

Discussion: Alternative Approaches to the Derivation

The most widely cited derivation of these equations is that of McKenzie [1984]. His approach, following Drew [1971], is based on the formal structure of mixture theory, an area of applied mathematics that addresses multiphase flows in general. A model of porous flow and viscous compaction represents a special case in this context. General statements are written for the conservation of mass and momentum of each phase. These contain interaction terms: for the conservation of mass the liquid lost is equal to the solid gained, and for the conservation of momentum the force exerted by each phase on the other is equal and opposite. The form of this "interphase force" is then chosen so that the momentum equation for the liquid becomes Darcy's law. At this stage, McKenzie's momentum equations, (A20) and (A21), are exactly equivalent to our Equations (2.6) and (2.8) above, with slight differences in notation. McKenzie does not discuss the circulation or derive the form of the Stokes equation by which it is governed. This description is, however, implicit in the momentum equations for the separate phases.

Fowler [1985], in an independent derivation, assumes *a priori* that circulation is decoupled from the porous flow. Consequently, he does not need to present an equation for the force balance on the solid phase (as does McKenzie) or on the two-phase medium (as we do). Fowler's equations are equivalent to those that we use in Chapter 4 in numerical experiments without circulation.

Scott and Stevenson [1986] present a derivation based on the conservation of energy rather than momentum. The balance of gravitational energy released and viscous dissipation in the two phases leads to the same system of equations governing porous low and compaction, but the process of circulation is not described. This approach would be more difficult if circulation were included, and also if the thermodynamics of the phase change were introduced. The equations governing the phase change are of a familiar form, there being little effect of the dynamics on the phase change. Both McKenzie and Fowler present suitable equations. The interaction between melting and magma ascent is discussed in Chapter 3.

Slight differences exist in the constitutive relation proposed in each of these derivations. We have stressed that this is not of great importance, but some clarification is appropriate. McKenzie does not introduce the factor of $(1 - f)$ that we include here in Equation (2.3) for constant matrix viscosities. Later in his derivation this factor is absorbed into the otherwise constant viscosities, simplifying the equations. In Scott and Stevenson [1986] we also omitted the factor of $(1 - f)$ in the constitutive relation, and by leaving it out later in the derivation produced a more complicated form of the governing equations. Fowler chooses an f^{-1} dependence for the bulk viscosity, based on a microscopic model that is equivalent to the pipe flow in Chapter 1.

CHAPTER 3

MAGMA ASCENT BY POROUS FLOW

Abstract

Porous flow of buoyant liquid through partially molten rock is regarded as the initial transport process leading to magma segregation in the mantle. The influence of the deformation and compaction of the matrix on this process is described by a generalized form of Darcy's law. Numerical experiments and analysis focus on the existence of solitary wave solutions, called magmons. These waves are regions of locally high porosity that ascend through regions of low, uniform porosity. In collisions, the individual magmons are very nearly conserved. Although the quantification of the relevant permeability and rheological parameters remains uncertain, geophysically plausible estimates suggest wavelengths of kilometers and velocities of centimeters per year. In our preliminary assessment of the relevance of these results to igneous processes, we find that magmons are unlikely to be important in regions of broad upwelling, such as beneath spreading centers. Here the transport of liquid adjusts to match the supply by melting, and compaction processes are not important. If liquid is supplied from below to a stable partially molten region of the asthenosphere, it is expected to ascend in magmons. Magma ascent in magmons may lead to

spatial and temporal episodicity of volcanic activity, if higher level processes do not obscure their influence. The principal geochemical effect of magmons is that they can mobilize small degrees of partial melt and deliver it rapidly to the surface.

Introduction

In light of the experimental observations of pipe flow described in Chapter 1, and the analogies between pipe flow and the mathematical model of porous flow developed in Chapter 2, the basic conclusion of this chapter will be that solitary waves may participate in the transport of magma in the Earth. The consequence of this prediction is that the unobserved processes of magma segregation and ascent may be indirectly observable through their influence on igneous products. This would not be possible if the process of ascent had less character: a mundane behavior would have no effect on observations, and a chaotic behavior would only add noise.

To refer to these unique and potentially important solitary waves in the Earth we propose the term "magmon," a contraction of "magma soliton." In this chapter we describe the behavior and consequences of magmons in the Earth through a mixture of numerical experimentation, mathematical analysis, and geophysical discussion.

Numerical Experiments in One Dimension

These experiments were performed using the non-dimensionalized, one-dimensional form of the governing equations derived in Chapter 2. The assignment of physical dimensions to the results presented is reserved for a later section.

$$w = f^{n} [- 1 + (f^{-m} w_z)_z] \qquad (3.1)$$

$$f_t = w_z \qquad (3.2)$$

Equation (3.1) is Darcy's law modified to include the effect of matrix deformation; Equation (3.2) is the statement of continuity. Comparing (3.1) with (2.24a), note there is no circulation. The only circulation that can occur in one dimension is a uniform translation of the whole system up or down. As in (2.29), we have introduced function dependencies of both the permeability and the matrix viscosity on porosity, parameterized by the exponents n and m. Recalling the discussion in Chapter 2, we expect $n = 2$ or 3, and $0 \leq m \leq 1$.

A sample of the many experiments that have been performed on this system are presented in Figures 3.1 and 3.2. The captions to these figures are self-explanatory, but the overall purposes of these experiments are stated here.

Firstly, we can simulate the pipe flow experiments. This is useful because we perform experiments that otherwise would be very difficult. The calculation in Figure 3.1 uses the exact form of the pipe equations, and shows solitary waves on a pipe that would be too thin to realize in the laboratory.

Secondly, we can investigate the effect of using differing constitutive assumptions to describe the microscopic properties of the porous medium. In the introduction to Chapter 2 we identify this effect as a substantive difference between pipe flow and porous flow. The values of both n and m used in Figure

Text continues on page 44

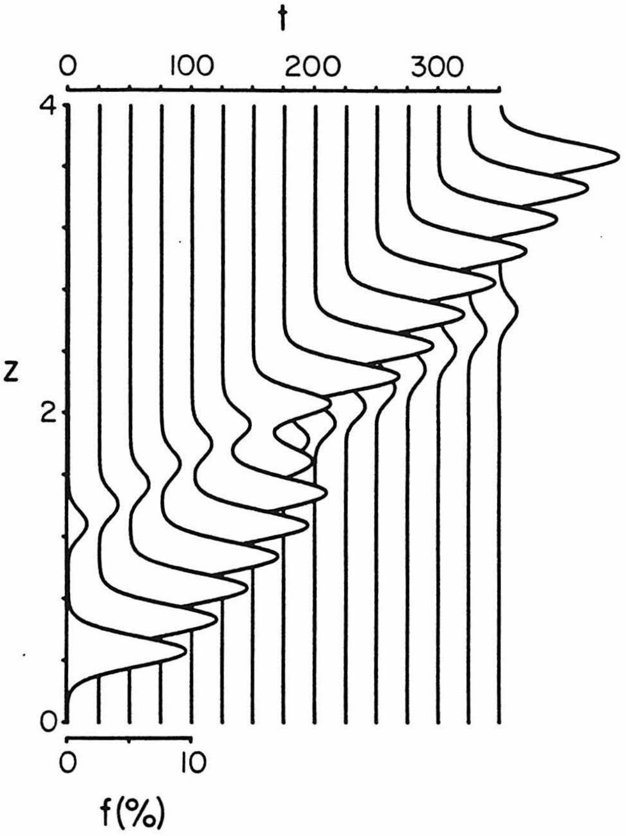

Figure 3.1. The interaction of two solitary waves. Vertical profiles of porosity are shown at successive points in non-dimensional time, as indicated by the upper horizontal axis. In this calculation, we use n = 2 in the matrix permeability and m = 1 in the effective matrix viscosity. These choices correspond to pipe flow, with porosity corresponding to the square of the pipe radius. The initial state consists of two solitary waves (approximately Gaussian when m = 1) in a column containing a uniform background liquid fraction of 0.1%. The flux at the upper and lower boundaries is prescribed to maintain this background value. If alone, the individual waves would ascend through the column at a constant velocity with unchanging form. Here, the larger wave ascends faster due to its greater total buoyancy, and overtakes the smaller. Both emerge essentially unchanged by the interaction, apart from the phase shifts seen in the plot. The background porosity is also unchanged, despite the large relative amplitude of the waves.

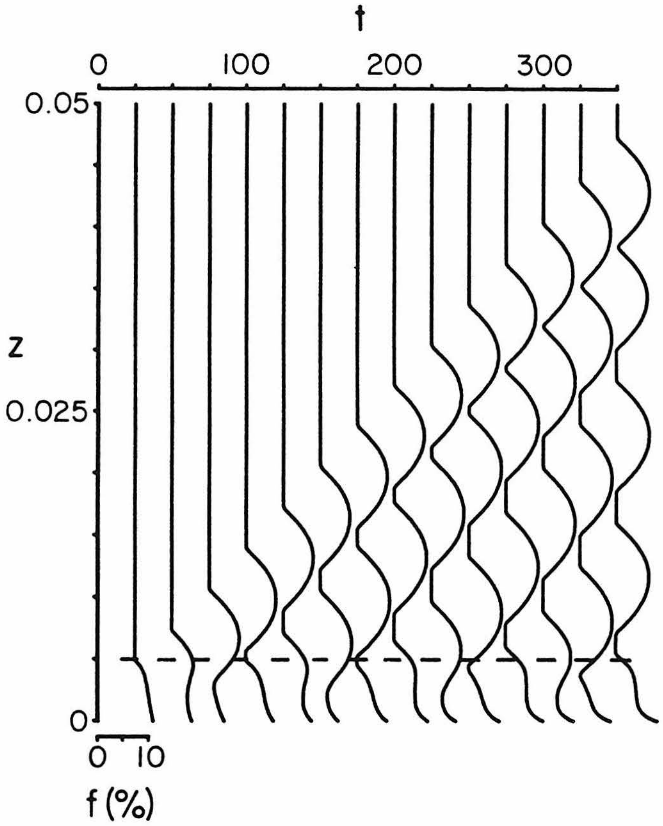

Figure 3.2. Creation of a wave train by a melting event. Layout of the plot is as in Figure 3.1. This calculation uses an n = 3 permeability and a constant (m = 0) effective matrix viscosity. Compared to Figure 3.1, these choices give smaller wavelengths and approximately parabolic wave profiles. Initially the column contains only a background liquid fraction of 0.1%. Melting then occurs in the lowest tenth of the column, below the dashed horizontal line, and continues at a constant rate. This simulates the pressure-release melting of a rock that consists of a low-melting fraction and a refractory residue. Solitary waves rise individually, separated by necks where the porosity returns to its background value. Note that the first wave has a slightly lower amplitude and velocity than the second. The latter catches up and in the last few profiles the type of interaction shown in Figure 3.1 is occurring.

3.2 are different from those representing pipe flow.

Thirdly, it is relatively easy to introduce other physical processes and study their effects. The melting in Figure 3.2 is an example. We have also investigated the effects of surface tension, non-linear rheology, and a depth-dependent density contrast (these are not discussed further).

Fourthly, we lay the numerical groundwork for the simulation of multi-dimensional porous flow presented in Chapter 4. The numerical method is described in the Appendix.

Analysis of Solitary Waves in One Dimension

Numerical experiments are of great value in investigating situations that are complex enough to mimic the real world. Our confidence in the numerical method is founded on careful testing, but more importantly on the mathematical analysis presented below. This analysis demonstrates that solitary waves should exist, and that the experimentally observed waves have the correct shape and speed.

We can seek solitary wave solutions that propagate over a constant, low background porosity f_0. Following the usual strategy [Drazin, 1983], we substitute a general traveling wave of porosity in Equations (3.1) and (3.2).

$$f = \phi(y), \qquad y \equiv z - c\,t \tag{3.3}$$

The unknown constant c is the ascent velocity of the wave. The object of this analysis is to find both the wave profile ϕ and the velocity c. Integration of (3.2) gives

$$w = w_0 - c\,\phi\,, \tag{3.4}$$

where w_0 is a constant of integration. In the background region, as $y \rightarrow \pm \infty$, we require that the porosity assume the constant value $\phi = f_0$. Also, for the waveform to be localized around $y = 0$, we require that $\phi_y = \phi_{yy} = 0$ in the background region. The asymptotic form of (3.1) is then

$$w_0 - c\, f_0 = - f_0^n \, , \tag{3.5}$$

which can be solved for the constant w_0. Substitution of (3.3), (3.4) and (3.5) into (3.1) gives the following differential equation in ϕ.

$$\frac{[c\,(\phi - f_0) - (\phi^n - f_0^n)]}{\phi^n} = c\,(\phi^{-m}\, \phi_y)_y \tag{3.6}$$

This can be integrated once using the following identity.

$$(\phi^{-m}\, \phi_y)_y \equiv {}^1\!/_2\, \phi^m \frac{d}{d\phi}\, [\phi^{-2m}\, \phi_y^2\,] \tag{3.7}$$

In the case $m = 0$, $n \neq 2$ we obtain

$$\phi_y^2 = \left(\frac{2\, f_0}{c}\right) \left[\frac{c^*}{(n-1)\,(n-2)} - \psi + \frac{n}{(n-1)} - \frac{c^*}{(n-2)\,\psi^{n-2}} + \frac{(c^* - 1)}{(n-1)\,\psi^{n-1}}\right] , \tag{3.8}$$

where $c^* = c \,/\, f_0^{n-1}$, and $\psi = \phi \,/\, f_0$. The new variables c^* and ψ are the ascent velocity and profile of the wave scaled to the ascent velocity of the background liquid and the background porosity. In the special case of n = 2, the expression inside the square bracket is replaced by

$$\left[c^* \left(\ln \psi - 1 + \frac{1}{\psi} \right) - \left(\psi - 2 + \frac{1}{\psi} \right) \right] . \tag{3.9}$$

Solitary wave solutions exist provided ϕ_y^2 (on the LHS of (3.8)) is positive for some finite range of ψ and goes to zero at some value of $\psi \neq 1$ as well as at $\psi = 1$. Geometrically, these conditions mean that the waveform must have zero slope both at the peak and in the background. We define the scaled wave amplitude Ψ as the maximum value of ψ, i.e., at the peak. These requirements stated above can be satisfied for $\Psi > 1$ ("positive" solitary waves) provided $n > 1$. This is a weaker constraint than our physical expectation that $n \geq 2$. The analysis can be repeated for the case m = 1 and again predicts solitary waves for $n > 1$.

Dispersion Relations. A dispersion relation for m = 0 can be obtained by setting $\phi_y = 0$ at $\psi = \Psi$ in Equation (3.8). For $n \neq 2$ this gives

$$c^* = (n-1)(n-2) \frac{\left[\Psi - \dfrac{n}{(n-1)} + \dfrac{1}{(n-1)\,\Psi^{n-1}} \right]}{\left[1 - \dfrac{(n-1)}{\Psi^{n-2}} + \dfrac{(n-2)}{\Psi^{n-1}} \right]} \tag{3.10}$$

and for n = 2,

$$c^* = \frac{\left[\Psi - 2 + \dfrac{1}{\Psi} \right]}{\left[\ln \Psi - 1 + \dfrac{1}{\Psi} \right]} . \tag{3.11}$$

The analysis for m = 1 leads to

$$c^* = n\,(n-1)\,\frac{\left[\ln \Psi - \dfrac{1}{n} + \dfrac{1}{n\,\Psi^n}\right]}{\left[1 - \dfrac{n}{\Psi^{n-1}} + \dfrac{(n-1)}{\Psi^n}\right]}\,. \qquad (3.12)$$

For all m, $c^* \rightarrow n$ as $\Psi \rightarrow 1$ (small amplitude waves), in agreement with the dispersion relation obtained by linearizing Equation (3.1). In analogy with the Korteweg-de Vries equation, it is found that the linearized frequency-wavenumber relation predicts dispersion but the non-linearity causes wave-steepening.

Wave profile. In Equation (3.8), ϕ_y is squared. Hence, while the value of the gradient is fixed given ϕ (or ψ), the sign is not. The wave profile must therefore be symmetric.

In the limit $\Psi >> 1$, Equation (3.8) can be integrated to give

$$\psi \approx \Psi - y^2 \,/\, 2\,c\,f_0 \qquad (\psi >> 1)\,, \qquad (3.12)$$

showing that the solitary waves are approximately parabolic when m = 0. Similarly, the approximate form when m = 1 is Gaussian:

$$\psi \approx \Psi \exp\,(-\,z^2 \,/\, 2c) \qquad (\psi >> 1)\,. \qquad (3.13)$$

For the particular case m = 0, n = 3, Richter and McKenzie [1984] have shown that the second integration (of Equation (3.8)) can be performed to give an implicit but exact expression for the wave profile.

$$\frac{y}{2\sqrt{2\,c\,\phi_{\max}}} = \frac{\sqrt{(1-\psi/\Psi)}}{2} + \frac{1}{4\sqrt{\Psi}\,(\Psi-1)}\ \ln\left(\frac{\sqrt{\Psi-1}+\sqrt{\Psi-\psi}}{\sqrt{\Psi-1}-\sqrt{\Psi-\psi}}\right) \tag{3.14}$$

The phase velocity takes a very simple form:

$$c = \phi_0^2\,(2\,\Psi+1)\,. \tag{3.15}$$

When written in this way the wavelength $\lambda = 2\sqrt{2\,c\,\phi_{\max}}$ is seen as the width of a parabola that approximates the profile.

Some insight into the ascent process can be obtained by studying the solid velocity profile for this case.

$$w = -\,[\phi_0^3 + c\,(\phi-\phi_0)] \tag{3.16}$$

In this one-dimensional case the liquid velocity is obtained from this solid velocity by multiplying by $(1-\phi)\,/\,\phi$. The prediction of the solid velocity from the algebraic form of Darcy's law is $w_D = -\,\phi^3$. The deviation from this prediction can be obtained using (3.15) and (3.16):

$$\frac{w}{w_D} = \frac{1+(2\,\Psi+1)\,(\psi-1)}{\psi^3}\,. \tag{3.17}$$

This expression is unity in the background ($\psi = 1$), less than unity at the peak ($\psi = \Psi$), but greater than unity at the edges of the wave. The physical interpretation of this result is that the large volume of liquid around the peak is unable to percolate at the full rate allowed Darcy's law, but it forces the liquid above and below to move more quickly than Darcy's law allows. The pressure difference between the phases is simply the derivative of the solid velocity, which from (3.16) is $- c\ \phi_z$. For the profile in (3.14), this is approximately equal to y in the body of the wave. This dipole of pressure difference drives dilation of the matrix in the upper half of the wave and compaction in the lower half.

Comparison with Experiments. The numerical and laboratory experiments show that the solitary waves are stable and arise spontaneously whenever excess liquid is supplied to the base of a column of constant porosity. The sizes and shapes of the observed waves are in agreement with the expressions for the wave profile presented above, and the ascent velocities agree with the theoretical dispersion relations. This agreement lends us confidence in the numerical method.

Other Published Analysis of the One Dimensional System. We have demonstrated that solitary waves exist; it is now of interest to establish how well they are conserved in collisions. To judge by Figure 3.1 the conservation is very good, but formally they should be called solitons only if they possess this property exactly. Whitehead and Helfrich [1986] have demonstrated that the equations governing pipe flow reduce to the Korteweg-de Vries equation in the limit of small wave amplitude. The well-known property of the KdV in admitting soliton solutions therefore applies to collisions between small $(\Psi \sim 1)$ waves when $m = 1$ and $n = 2$.

The more interesting large amplitude case has been addressed by Barcilon and Richter [1986], who investigate the case $m = 0$, $n = 3$. Although their analysis is incomplete, it suggests strongly that the waves are not solitons. They also document high-resolution numerical studies in which collisions result in a small residual disturbance in the background porosity. Our experience with both numerical and laboratory experiments is consistent with this imperfection and suggests that large waves always grow at the expense of smaller waves.

The conservation is, however, sufficiently good that the imperfections in the real world, compared to the mathematical model, will disturb the waves more than the mathematical imperfections arising when they collide.

Quantification

We are confident that the qualitative aspects of our results are robust. For this reason, the speculative assignment of physical dimensions to these results is reserved for this separate section. The importance of magma ascent by porous flow, and particularly in magmons, is, of course, dependent on such assignments. We present conservative estimates for the relevant material properties in Table 3.1, with some commentary on their selection in the footnotes. In this context "conservative" means tending to reduce the size and velocity of magmons.

The expressions for velocity and wavelength in the preceding section and all the scales in Figures 3.1 and 3.2 are non-dimensional. To obtain values for the Earth we simply multiply by the appropriate dimensional scale from Table 3.1. The generality of the analysis and numerical solutions is one of the main reasons for using non-dimensional equations.

Figure 3.3a-d show the variation of magmon ascent velocities c and half-heights h with amplitude. The velocity plots were produced using the one-dimensional dispersion relations derived above. The heights are the half-heights of approximate solutions to the one-dimensional equations:

$$h = [2\ c\ f_{\max}]^{1/2} \quad (m = 0), \qquad h = [2\ c]^{1/2} \quad (m = 1)\,. \qquad (3.18)$$

Text continues on page 54

Table 3.1.

Parameter	Symbol (Definition)	Value		Units
Porosity	f			none
Matrix viscosities[i]	ς, η	10^{19}		Pa s
Liquid viscosity[ii]	η^{liq}	10		Pa s
Gravity	g	10		$\mathrm{m\ s^{-2}}$
Density contrast[iii]	$\Delta\rho = \rho^{\mathrm{sol}} - \rho^{\mathrm{liq}}$	100		$\mathrm{kg\ m^{-3}}$
Grain radius	a	10^{-3}		m
Permeability[iv]	$k = a^2\, f^{\,n} / b$			$\mathrm{m^2}$
	n	2	3	none
	b	10^4	10^3	none
Length scale[v]	$L = a\left[(\varsigma + {}^4\!/_3\eta) / b\ \eta^{\mathrm{liq}}\right]^{1/2}$	10	30	km
Time scale	$T = \dfrac{1}{g\ \Delta\rho\ a}\left[(\varsigma + {}^4\!/_3\eta)\ b\ \eta^{\mathrm{liq}}\right]^{1/2}$	3×10^4	10^4	yr
Velocity scale[v]	$L / T = g\ \Delta\rho\ a^2 / b\ \eta^{\mathrm{liq}}$	30	300	$\mathrm{cm\ yr^{-1}}$

This table shows various material properties, all of which influence the values of the length, time, and velocity scales used to non-dimensionalize the governing equations. In light of the quantitative uncertainties, a preference for round numbers was a significant factor in the choice of values for these properties.

(i) See Chapter 2 for discussion of the matrix rheology.

(ii) Basaltic liquid. See Kushiro [1986].

(iii) A relatively low value has been chosen, in light of the decrease of density contrast with depth [Rigden *et al*, 1984].

(iv) The choices of the parameters n and b in the permeability provide two fits to the data of Maaløe and Scheie [1982]. See Chapter 2 for discussion.

(v) We consider the numerical values given for the length and velocity scales to be lower bounds because of our conservative choices for the grain size and density contrast. Note that the velocity scale varies as the square of the grain size.

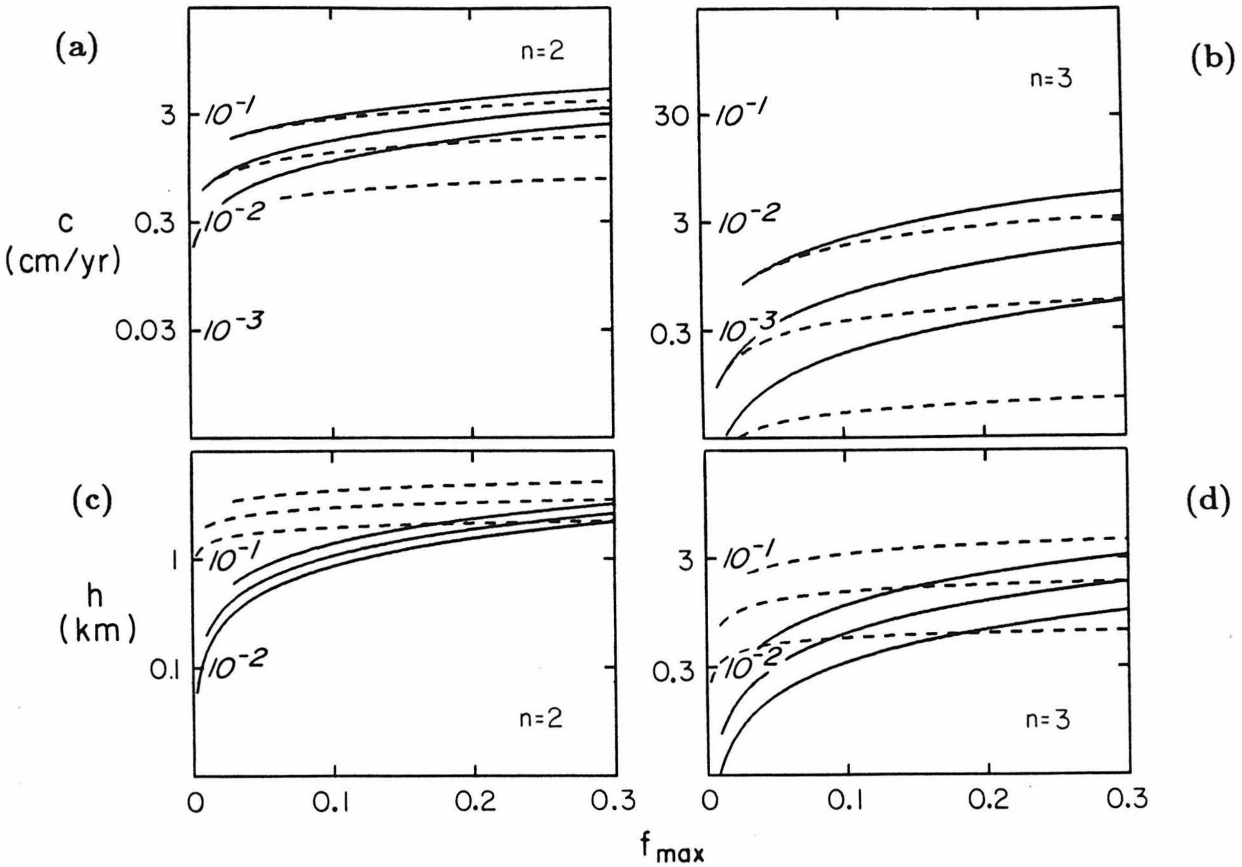

Figure 3.3. Magmon heights and ascent velocities. These plots show the ascent velocity and approximate half height of magmons for a range of parameter choices. Figures 3.3a and 3.3b show the ascent velocity c plotted against the maximum amplitude f_{max} of the waveform, on log-linear axes. In Figure 3.3a, $n = 2$ is used for the permeability; in Figure 3.3b, $n = 3$ is used. For the solid lines, $m = 0$ is used for the matrix viscosity; for dashed lines, $m = 1$ is used. In each case, three values of the background porosity f_0 are used; $f_0 = 3\%$, 1%, and 0.3%. The larger values of f_0 correspond to larger values of c. The vertical axes have two calibrations; the italic numerals within the axes are the non-dimensional values of c, and the roman numerals are dimensional values, in centimeters per year. Note that the dimensional calibration is different on Figures 3.3a and 3.3b because the velocity scale in Table 3.1 is different for $n = 2$ and $n = 3$. Figures 3.3c and 3.3d show the half heights of magmons, for the same range of parameters as Figures 3.3a and 3.3b. Again, the dimensional calibration is different for $n = 2$ and $n = 3$.

The approximation is good in the large-amplitude limit and provides a lower bound for small amplitudes. The conclusion from these calculations is that magmon half-heights of at least 1 km, and magmon velocities of at least 1 cm/yr, are to be expected. The volume of liquid within a magmon of this size, with an amplitude of about 10%, is about 1 km^3. The maximum value of the pressure difference between the liquid and solid matrix is a few bars.

Discussion: Melting and Magma Ascent

The focus of this discussion is an assessment of the likely importance, in the Earth, of magma ascent in magmons. We must first discuss the incorporation of the actual melting into our modeling of magma ascent.

The actual process of melting is not included in the equations we have been modeling. We justify our study of the system without the inclusion of melting as follows. Coupling the melting process into the system has two effects: (1) The addition of an equation for the conservation of energy, balancing the heat capacity and the latent heat of melting. This is coupled to the momentum equations by the heat supplied from viscous dissipation, but this is a small term. (2) The addition of a source term in the continuity equation, representing the time derivative of porosity due to melting. This is controlled by the energy equation above, but not by the dynamics of porous flow and compaction. This source term dominates the coupling between melting and magma migration.

We identify two end-member regimes, in which the nature of magma ascent by porous flow is very different. The first is that in which the flow process is dominated by the rate of supply of liquid by melting throughout the region of interest. As discussed below, this regime probably exists beneath spreading centers. The second regime is that in which liquid is supplied to a stable partially molten region from below, and this supply dominates over melting within the region itself. This condition may exist in regions of the asthenosphere away from spreading centers, when liquid is supplied from below. In this case, magma is expected to ascend in magmons.

The transition between these two end-members may be quantified as follows. For a magmon to retain its identity, the background liquid fraction f_0 must change slowly relative to the rate of ascent of the magmon. Expressing as an inequality, we obtain

$$\frac{1}{f_0} \frac{Df_0}{Dt} << \frac{c}{h} . \tag{3.19}$$

The usefulness of this inequality has been demonstrated by experimentation on the one-dimensional system of equations, with melting included. If we attribute the melting Df_0 / Dt to adiabatic ascent of the partially molten rock as a whole at velocity W, we find

$$W << 3 \text{ cm yr}^{-1} . \tag{3.20}$$

We have taken $n = 3$, $m = 0$, $f_0 = 1\%$, $f_{max} = 10\%$, and 0.3 %/km as the adiabatic rate of melting. We conclude that magmons can survive only in partially molten regions of the mantle that are not undergoing significant ascent.

The problem of melting due to steady, adiabatic decompression was originally addressed by Turcotte and Ahern [1978] and has been reviewed by Ribe [1985] in the light of recent work on porous flow and compaction. The conclusion is that in the scenario of a broad mantle upwelling beneath a spreading center, compaction is not important because the rate of magma escape adjusts to match the rate of magma production. In this setting, the thermal structure is dominated by the buffering effect of the phase change. Heat transfer by conduction is negligible within the melting regime, and heat transfer by movement of the magma is tempered because the magma is everywhere in intimate thermal contact with the matrix. To this we should add that due to the pervasive nature of the melting, magma ascent in magmons is unlikely to occur beneath ridges. McKenzie [1985] and O'Hara [1985] provide examples of how to relate petrological and geochemical observables to processes in the mantle beneath ridges.

If magmons exist anywhere, they should have some impact on geological observables. A simple suggestion is that the episodicity of the ascent process may translate into episodicity in the emplacement of the magma at or near the Earth's surface. The episodic ascent could cause either temporal or spatial periodicity in emplacement. However, we do not propose that porous flow delivers magma all the way to the Earth's surface. Therefore, it is not clear that the associated periodicity could be detectable after the operation of high-level transport processes.

Magmons exchange liquid with the background region as they ascend, as illustrated in Figure 3.4. (We also describe the exchange of liquid between large and small solitary waves during collisions in the caption to Figure 4.3). Consider the velocities of the waveform and of the liquid at various points. In the background region, the liquid ascends uniformly at the Darcy flow velocity corresponding to f_0. The waveform ascends faster than the background (the relative velocity is the quantity c^* defined earlier). The ascent velocity of the liquid is greatest at the peak of the wave but is still less than that of the waveform. Consequently, the waveform takes in new liquid from above and loses its original liquid from below. The rate at which this replacement proceeds depends on the amplitude of the wave; a larger wave will need to traverse more background liquid before it fills up. We note that flow of liquid through the matrix always follows streamlines, meaning that mixing between

Text continues on page 58

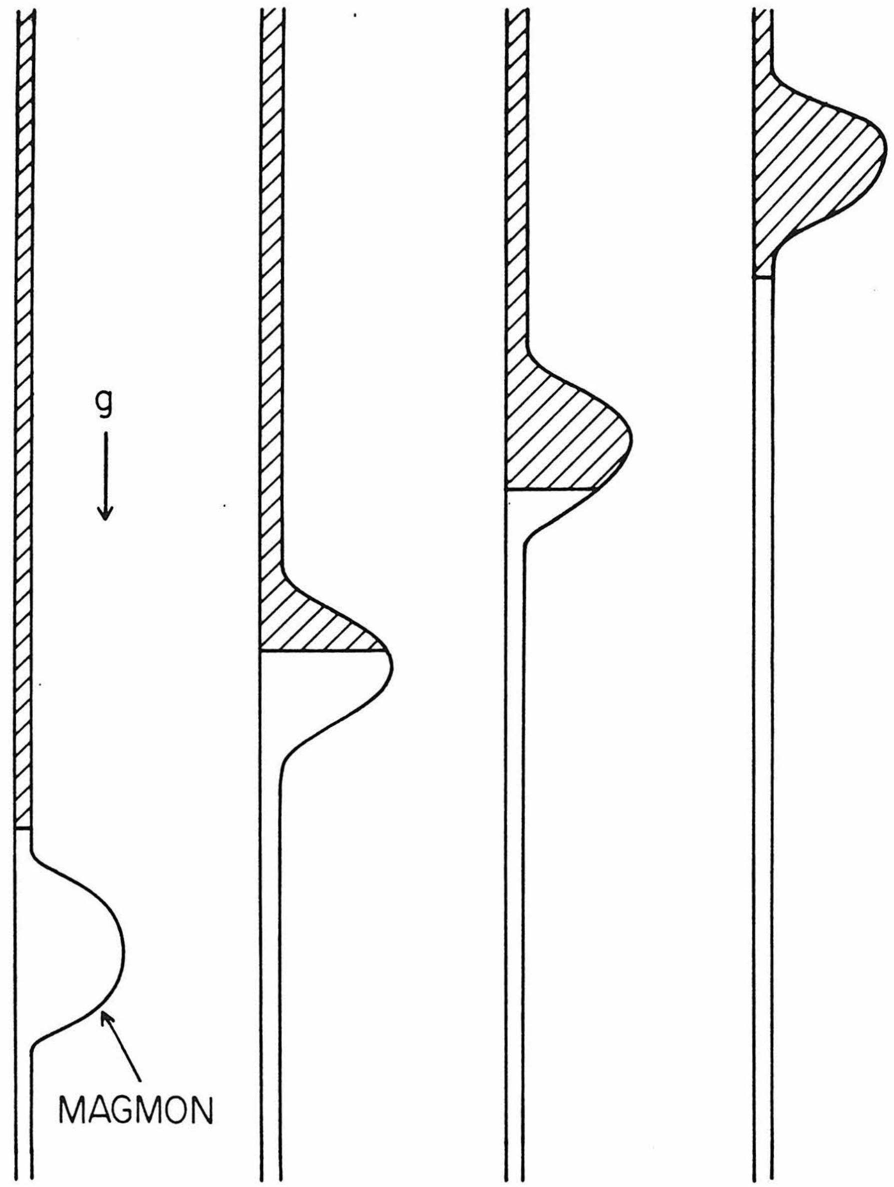

Figure 3.4. A schematic one-dimensional experiment showing the exchange of liquid between a magmon and the background. See text for discussion.

the different liquids does not occur, even within the wave. This statement should be qualified; percolative dispersion will gradually blur a boundary between two fluids such as that in Figure 3.4.

This exchange has interesting implications for the chemical characteristics of magma delivered from a magmon. Suppose that a magmon ascends through a region where the liquid in the background is in equilibrium with the matrix. As the original liquid in the magmon is replaced with liquid from the background, this new liquid will remain in equilibrium with the matrix. This is because the equilibrium depends on concentrations; the effect of the passage of a magmon is to change only the volume fraction of liquid by collecting liquid from a vertically extensive region into one place. Conversely, the liquid originally in the magmon is left spread out in the trail of the magmon. This result applies to both major and trace elements. The effect is that if the background liquid has a chemical signature corresponding to a small degree of partial melting, the magmon will deliver a large volume of this liquid in a short time. This process is akin to zone refining, which Harris [1957] has proposed to explain the origin of alkali basalts. We prefer to emphasize the more general conclusion that caution is needed in deducing source region sizes and time scales for magma escape, from petrological and geochemical observations. The fate of the liquid in the trail of the magmon is also of interest because it may be in disequilibrium with the matrix. The work of Navon and Stolper [1986] addresses this effect, making the analogy with a chromatographic column.

Our discussions of the conditions for survival of magmons, the possible effect on the periodicity of igneous emplacement, and the mechanism by which small degrees of partial melt may be collected and mobilized, can guide the hunt for magmons in the Earth. A candidate tectonic setting must have a suitable pattern of melting and flow in the mantle and igneous activity with the appropriate physical and chemical characteristics. We suggest that magma ascent in magmons may occur beneath hot spots, magmatic arcs over subduction zones, or seamounts on the periphery of spreading centers. In all these settings, there is the prospect of regions of melting below regions that are partially molten but that are either stagnant or only moving laterally. The igneous rocks show geochemical complexities that imply mixing of magmas and smaller degrees of partial melting than are seen at ridges. The testing of these assertions will require less idealized fluid dynamical modelling (we move towards this in Chapter 4), and the re-examination of geological observations in the light of this modeling.

To this we add that it would be surprising if Nature did not, at some time and place, take advantage of this robust and distinctive phenomenon.

CHAPTER 4

SOLITARY WAVES IN MULTIDIMENSIONAL POROUS MEDIA

Abstract

We present two series of calculations that model the dynamics of a partially molten region. The first series are finite-difference calculations based on a generalized form of Darcy's law that includes matrix deformation but not circulation of the two-phase medium. They focus on the existence of solitary wave solutions, called magmons, in two-dimensional Cartesian and cylindrical geometries. These waves are regions of locally high porosity that ascend through regions of low, uniform porosity. They differ from diapirs, where the liquid and matrix ascend together. The one-dimensional waves that were reported previously are found to be unstable in two dimensions, breaking down to form two-dimensional waves of circular cross section. Numerical experiments in which two-dimensional waves collide show that the extent to which they are conserved after collision depends on the lateral offset of the waves. The conservation can be very good; in other cases, larger waves appear to grow at the expense of smaller waves. A second series of calculations uses a hybrid combination of finite-difference and finite-element techniques to investigate the behavior of magmons when circulation is allowed. In two-dimensional Cartesian geometry, solitary waves of circular cross-section persist. This conclusion holds even if the shear viscosity of the matrix is lowered relative to the bulk viscosity, to encourage diapiric ascent. The form of the two-dimensional waves, both with and without circulation, is supported by theoretical analysis. The superposition of magmons and large scale diapiric instabilities in a partially molten region is discussed.

Introduction

Our main interest has been in studying the behavior and stability of the solitary wave solutions described in Chapters 1 and 3 for the one-dimensional case. The one-dimensional solitary waves consist of regions of locally high liquid content that ascend over a constant, lower background porosity. In the upper half of the wave, the matrix dilates in response to the arrival of more liquid than can be accommodated by Darcy flow. Symmetrically, the matrix compacts in the lower half. The wave is therefore accompanied by a dipole of pressure difference between the liquid and matrix. The passage of the wave leaves no disturbance in the amplitude of the background porosity. Furthermore, the solitary waves behave, to a very good approximation, as solitons; this means that the individual waves are conserved in collisions between waves. Such collisions arise because the ascent velocity of the waves increases with the amplitude of the wave.

In deriving the governing equations in Chapter 2, we emphasised the existence of two independent flow fields in multiple dimensions: the porous flow and the circulation. This theme is developed in this chapter. We demonstrate that considerable advantage is derived from representing the system in this way, in both numerical modeling and analysis. In particular, we conclude that the circulation, and the interacting processes of porous flow and compaction, are largely decoupled.

Numerical Experiments without Circulation

The numerical study of the governing equations has now been extended to two spatial dimensions, for both Cartesian and cylindrical coordinates. This series of calculations adopt an approximation in which circulation is not permitted. The main justification for this approximation is that it allows us to examine the interaction between porous flow and compaction in a simplified multidimensional system. The equations needed to describe the system reduce to Darcy's law (2.10), with $\mathbf{V}^{\mathrm{com}} = 0$, and the compaction Equation (2.16). Some notes on the numerical method are presented in the Appendix.

Recalling the considerations of matrix viscosity and permeability discussed in Chapter 2, we must prescribe the functional dependence of these quantities on f. The studies of the one-dimensional system in Chapter 3 show that varying these dependencies altered the results quantitatively. Qualitative aspects, notably the existence of solitary waves, are unaltered. We have therefore chosen to concentrate on a specific case for the two-dimensional experiments:

$$\mathrm{k} = \mathrm{f}^3 \ \ (\mathrm{n} = 3) \qquad \varsigma = \eta = \mathrm{const} \ \ (\alpha = {}^3\!/_7) \, . \tag{4.1}$$

This case proves to be the most analytically tractable within the physically reasonable range of choices. The constant viscosities correspond to the choice m = 0 in Chapter 2 (see Equation (2.29)).

The numerical experiments shown in Figures 4.1, 4.2 and 4.3 were performed to address three specific issues that arose from the identification of solitary wave solutions in one dimension.

1. What is the fate of one-dimensional solitary waves in two dimensions? Referring to Figure 4.1, we see that the one-dimensional waves are unstable in two dimensions, breaking down in the time it takes to ascend several times their

own height. A linear stability analysis pertaining to this experiment is presented in Scott and Stevenson [1986], which demonstrates that the growth rate of the instability in the experiment is consistent with the analytic prediction.

2. Do solitary waves exist in two dimensions? Stable solitary waves of approximately circular cross section exist in two, and probably three, spatial dimensions. Their development from a one-dimensional solution is seen in Figure 4.1. The waves used in the initial states in Figures 4.2 and 4.3 are all solitary waves, preserving their shape and amplitude during ascent. These experiments are not, however, conclusive; the final answer is reserved for experiments that include circulation, described below.

3. Do two-dimensional solitary waves share the approximate soliton behavior of the one-dimensional waves when they collide? The collisions shown in Figures 4.2 and 4.3a-c show that they retain some of their identity. In particular, a large and fast-moving wave survives collisions with smaller waves quite well. It may be that large waves tend to pick up liquid from smaller waves, but this hypothesis requires further testing. This has been the case in all the numerical and laboratory experiments where any change in wave amplitudes could be detected.

Text continues on page 68

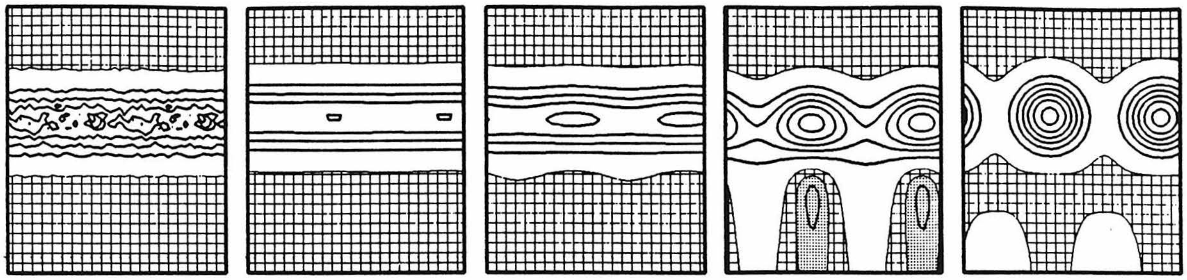

Figure 4.1. The development of two-dimensional solitary waves. Each frame is a contour plot of liquid fraction in two-dimensional space. The contouring scheme is as follows: the checked pattern shows values within 2% of $f_0 = 0.01$; the white area shows higher values, contoured with an interval of 0.2 f_0; values less than 98% of f_0 are stippled, and contoured with an interval of 0.02 f_0, one-tenth of that in the white areas. This scheme is designed to illustrate the gross behavior of the system and any small fluctuations about f_0. T experiment is performed on a two-dimensional Cartesian grid using Equatic (2.24a,b) without circulation; the numerical method is described in the Appe dix. The lateral boundary conditions are periodic; each frame shows two perioc for clarity. The grid scrolls upward, ascending 1.56 times the frame heigh between each frame. The initial state, shown in the first frame, is a one-dimensional solitary wave with white noise added to the waveform (but not to the background value f_0). This distribution is unstable in two dimensions; the liquid localizes laterally as the waveform ascends. The width of the grid was chosen after we performed an experiment on a wider grid to establish the preferred lateral wavelength of the instability. The nondimensional height of each frame is 0.06. The total elapsed time is 800. The nondimensional ascent velocity of the frame is 4.7×10^{-4}.

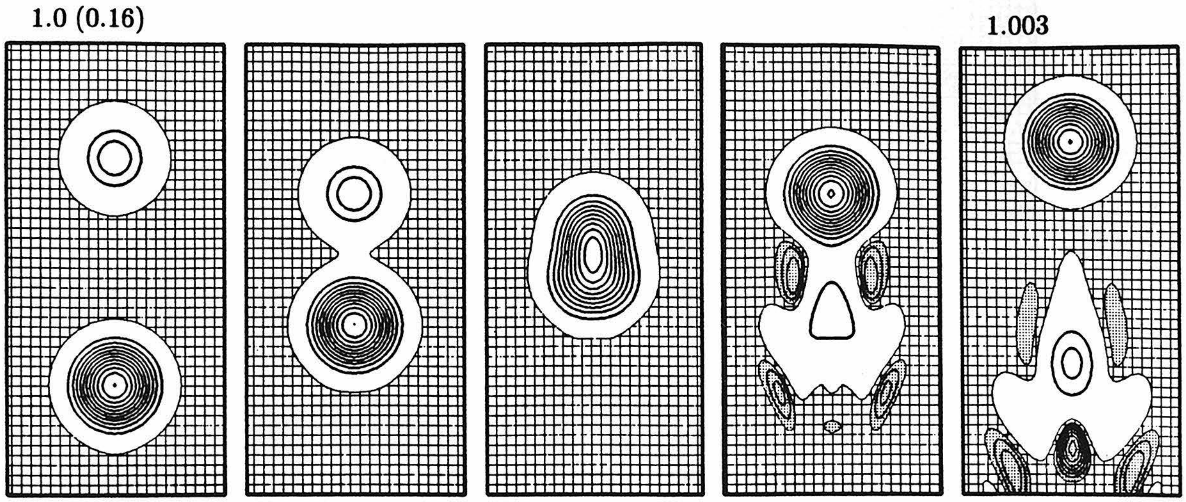

Figure 4.2. A collision of cylindrically symmetric solitary waves. This sequence shows an experiment in cylindrical polar coordinates with no azimuthal variation, simulating an axially symmetric three-dimensional system. See Figure 1 for the contouring scheme; the only change is to the contour interval in the white areas, which is 0.25 f_0. The experiment was performed in half the region shown in the plot, with symmetry boundary conditions across $r = 0$. Equations (2.31a,b) were used, without circulation. The initial state consists of two spherical solitary waves, which when taken individually ascend unchanged through a region of uniform liquid fraction. The numbers above the first frame are the volumes of liquid in the large and small waves, scaled to the volume of the large wave. The number above the last frame is the volume of the large wave after the collision. The experiment shows that the collision conserves the shape and volume of the large wave very well. The smaller wave is disturbed but retains its identity. The uniform background is also somewhat disturbed. The axial symmetry means that this collision is necessarily perfectly centered. The nondimensional height of each frame is 0.12. The total elapsed time is 480. The frame ascends 0.45 times the frame height between each frame, a nondimensional ascent velocity of 4.5×10^{-4}.

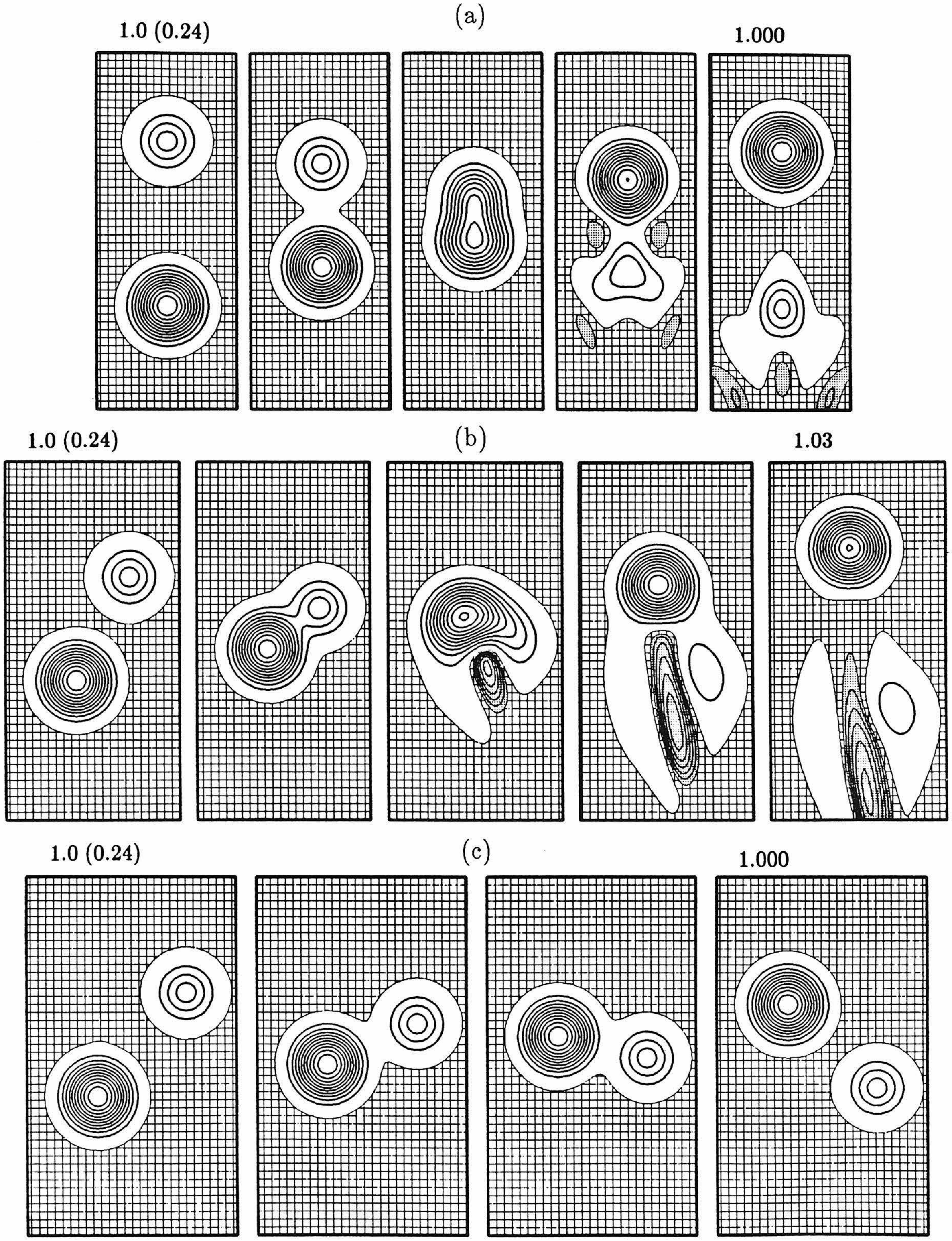

Figure 4.3. Centered and offset collisions in two dimensions. The contouring scheme is the same as that in Figure 4.1. These experiments are in

two-dimensional Cartesian coordinates with periodic boundary conditions, and use Equations (2.24a,b) without circulation. The three sequences show the same pair of solitary waves, one large and one small, colliding when centered (Figure 4.3a) and with two offsets (Figures 4.3b,c). The centered collision shown in Figure 4.3a resembles the pseudo-three-dimensional collision in Figure 4.2 quite closely, lending us some confidence in the relevance of two-dimensional experiments. As in Figure 4.2, note the good conservation of the volume of the larger wave. In Figure 4.3c the lateral offset between the two waves is large enough for them to pass without interacting significantly. There is, however, a significant difference between the end results in Figures 4.3a and 4.3c. In Figure 4.3a the liquid within the small wave is absorbed into the large wave; the large wave loses an equivalent volume from its base, which reforms as a new small wave. In Figure 4.3c, there is no such exchange. The intermediate case is shown in Figure 4.3b. The large wave is shifted laterally during the collision; it also emerges with 3% more liquid (about 8% of the smaller wave). The small wave is severely distorted, and a second small wave is left in the wake of the large wave. They are separated by a strip depleted to about 90% of f_0. The remnant of the small wave contains its original liquid (as in Figure 4.3c), and the new small wave contains liquid lost from the large wave (as in Figure 4.3a). The non-dimensional height of each frame is 0.12. The total elapsed time is 480 for Figures 4.3a,b and 248 for Figure 4.3c. The frame ascends 0.41 times the frame height between each frame, a non-dimensional ascent velocity of 4.5×10^{-4}.

Numerical Experiments with Circulation

The numerical study of porous flow without circulation described above provides considerable insight into the novel aspects of our overall model, i.e., the interaction between porous flow and compaction. In this section we acknowledge that there is no physical limit in which circulation can be ignored in the way that we have done above. We seek to build on our new insight by allowing circulation and determining its effect on the ascent of magmons.

First, we clarify the notion of circulation as a flow field that is independent of porous flow. Consider the interior of a permeable, partially molten region, away from boundaries with solid rock or with regions where some transport process other then porous flow operates. Magmons can ascend within this region: solitary waves of locally high porosity, propagating up through a column of uniform, low porosity. Any of the previous figures in this chapter illustrate this phenomenon. Now imagine closing off the permeable pathways through the rock and trapping the buoyant liquid in the solid matrix. The buoyancy distribution in a magmon would cause diapiric ascent of the whole rock around the peak of porosity. In this case the solid and liquid flow together and their common flow field, the circulation, is divergence-free. Such motions were excluded in the approximation used in the preceding part of this chapter.

As an alternative example, a circulation field could be imposed externally by applied stresses or velocities at the boundary of the region. Both the diapiric and externally driven flows have analogues in the familiar picture of large-scale mantle flow governed by the Stokes equation. The difference arises here because we are allowing porous flow to occur, superimposed on the pattern of circulation. The interactions between the two types of flow are quantified in the full form of the governing equations: Darcy's law (2.10) and the Stokes equation (2.15).

Numerical Experiments. By casting the governing equations in a form that explicitly displays the two types of flow, we have been able to develop a numerical scheme that exploits their physically different character. This is described in detail in the Appendix, but a qualitative description is included in the caption to Figure 4.4. That figure illustrates the model problem of a magmon in a large uniform region, solutions to which are presented in the subsequent figures. Numerical experiments on this model system were performed with two considerations in mind:

1. We now have good reason to believe that magmons are perfectly nondispersive if circulation is disallowed (although they are not perfectly conserved in collisions). The additional degrees of freedom introduced by circulation might be expected to introduce some dispersion, manifest in a degradation of the magmons as they ascend. Figure 4.5 shows the flow fields for a magmon that has retained its solitary wave character. Starting with the waveform for a magmon without circulation, we find that the profile changes slightly but then ascends with unchanging form, in the same way as any of the magmons in Figures 4.1, 4.2 and 4.3. The waveform remains circular to high accuracy, although the ascent velocity increases significantly. This experiment has been repeated for a number of different magmon amplitudes and background porosities.

2. The analysis presented above shows that the viscosity parameter α has surprisingly little effect on the solutions without circulation. Since the rate of circulation depends on the shear viscosity alone, we expect some change in the solutions with changing α when circulation is allowed. Figure 4.6 shows the solid velocity field for three values of α. In all three cases, the solitary wave behavior persists and the waveform remains circular. As expected, the phase velocity of the magmons acquires an increasing diapiric component as α decreases, amounting to more than 10% in the extreme case.

The development of two-dimensional waves (Figure 4.1) with circulation is being studied by Richter (personal communication). The character of the instability remains the same although the growth rate is faster than that predicted without circulation [Scott and Stevenson, 1986]. This increase is expected in light of the increase in ascent velocity when circulation is permitted (see caption to Figure 4.5).

The following descriptive explanation is offered for the persistence of magmons. As was stated in Chapter 2, the circulation appears in Darcy's law (2.10) only as a background variation. No derivatives of the circulation appear. In contrast, the interaction term **A** in the Stokes equation is strong, containing second derivatives of the porous flow field. However, the Stokes equation for incompressible flow tends to suppress the effect of rapid variations in the body force and always produces a smooth pattern of circulation. The processes described by Darcy's law are able to adapt to this smooth background variation in an "adiabatic" fashion, and so the porous flow retains its basic character.

In light of this explanation the success of the first series of calculations, where circulation was not included, appears reasonable. With hindsight we can justify that approximation, because the addition of circulation seems to have very little effect on the interaction between porous flow and compaction. Although the collision calculations in Figures 4.2 and 4.3 have not been repeated with circulation (because of computational limitations), it is very likely that our conclusions about the conservation of the magmons in collisions will remain valid. There may be some weak long-range interaction due to the patterns of circulation around the two magmons. At short range the interaction between the rapidly varying porous flow fields will be dominant.

Text continues on page 78

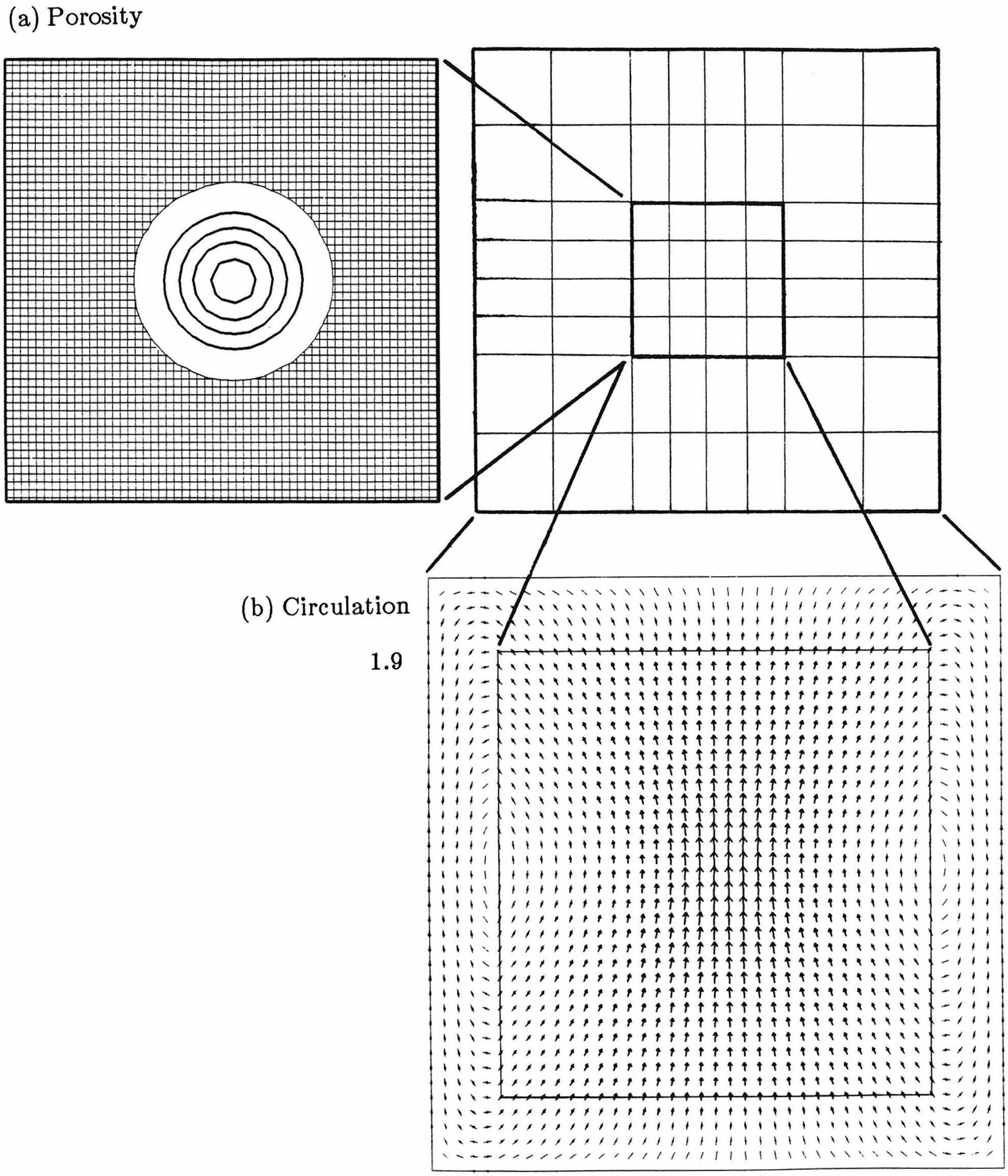

Figure 4.4. A magmon in a large uniform region. We wish to calculate the flow throughout the large box in 4.4a due to the magmon in the small box,

shown magnified to one side. The contour interval is 0.5% and the background porosity is 1%, so the peak porosity of the magmon is about 3%. We assume a uniform porosity of 1% outside this small box.

The porous flow $\mathbf{V}^{sol} - \mathbf{V}^{com}$ associated with ascent of the waveform by dilation and compaction is calculated only in the small box, with high resolution. We solve Darcy's law using the same finite difference method that was used for porous flow without circulation. Outside the small box we assume that the porous flow obeys the algebraic form of Darcy's law. The circulation $\mathbf{V}^{com}$ associated with diapiric ascent extends out into the large box, with free-slip boundary conditions at the outer boundaries. Outside the small box it is slowly varying and requires lower resolution. We solve the Stokes equation in both boxes simultaneously, using a finite element scheme. The scheme can accommodate the different sizes and shapes of element found in different regions of the two boxes. We iterate between the two calculations to obtain a consistent solution for the flow fields and then advance f in time.

The flow field shown in 4.4b is the circulation due to the buoyant region in the small box, if porous flow is not permitted. The shear viscosity correponds to $\alpha = 3/7$. The peak non-dimensional velocity is the number shown above the frame, multiplied by 10^{-6}. Velocities greater than 10% of this peak value are represented by a bold arrow at the node point, of length proportional to the velocity. The direction of flow at nodes with lower velocities is indicated by a light line. This scheme is intended to combine the advantages of a plot of streamlines with a clear representation of the variations in the magnitude of the velocity.

In this calculation and all those in subsequent figures, the non-dimensional size of the large box is 0.32 × 0.32, while the size of the small box (indicated by the inner line) is 0.06 × 0.06. The small box contains 30 × 30 elements (31 × 31 nodes), while the large box has an additional 5 elements in all directions. In displaying the flow field, the region outside the small box has been compressed so that the node spacing appears the same as that within the small box.

The flow field in 4.4b shows, as expected, an ascending region due to the buoyancy and the return flow at the sides of the large box required by continuity. Note that the vortices associated with this flow are outside the small box on either side. This pattern of circulation leads to the ascent of the buoyant region as a diapir, but not as a shape-preserving solitary wave.

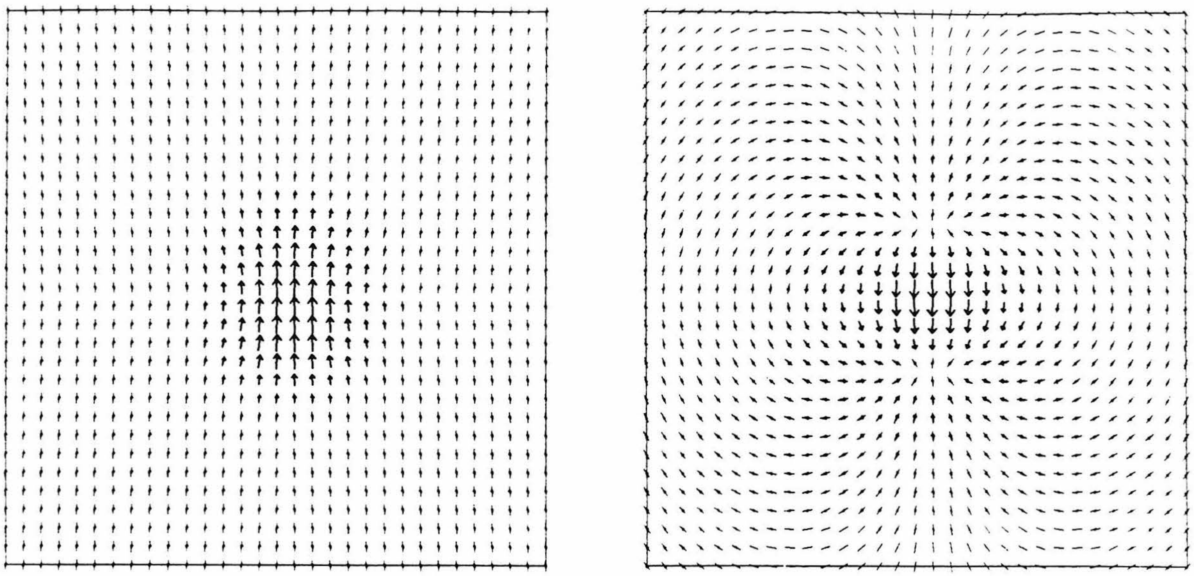

(a) Liquid 576

(b) Solid 7.5

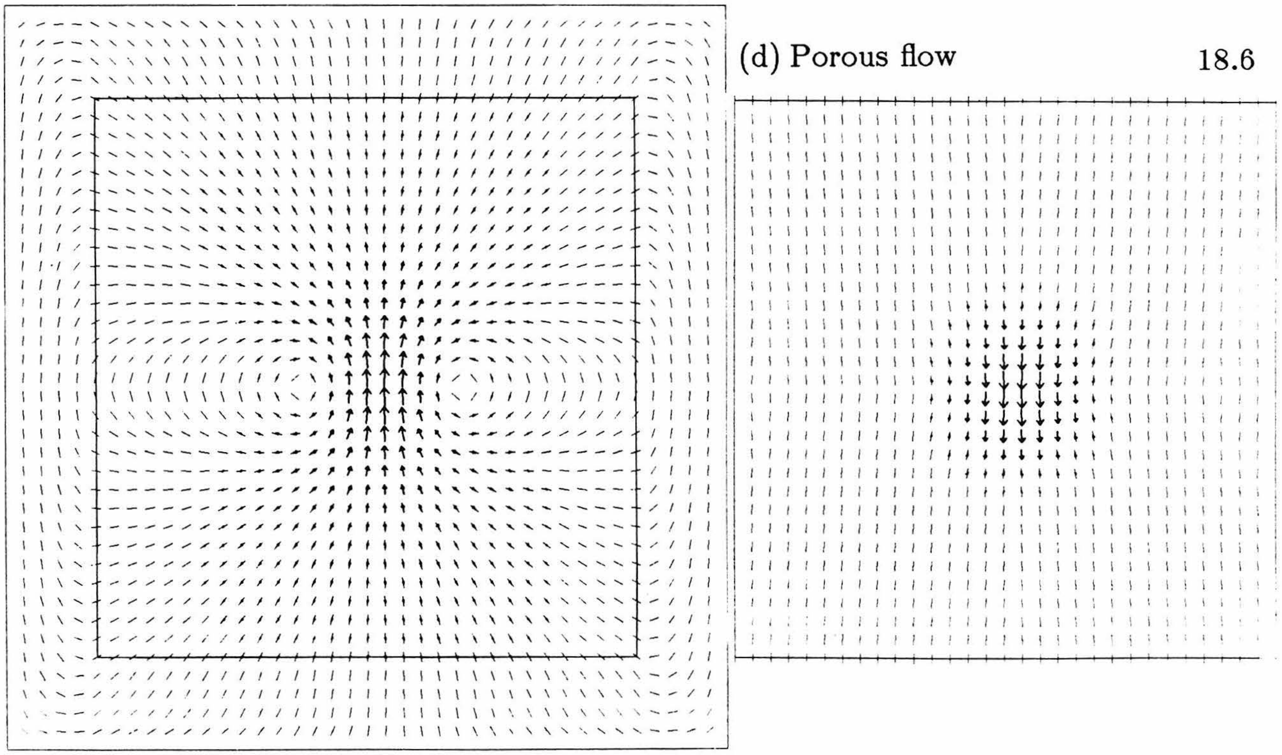

(c) Circulation 11.0

(d) Porous flow 18.6

Figure 4.5. Flow fields for $\alpha = 3/7$. The initial condition for this calculation is the magmon shown in Figure 4.4a. With both porous flow and circulation permitted, it is allowed to ascend and evolve. The grid scrolls upward, fol-

lowing the waveform. The waveform rapidly evolves to a steady state, a solitary wave of circular form. The porosity profile is so similar to that shown in Figure 4.4a that it is not illustrated separately. The flow fields shown here correspond to this steady state.

4.5a and 4.5b are the velocity fields for the liquid and solid, respectively. 4.5c is the circulation $\mathbf{V}^{com}$ and 4.5d is the porous flow $(\mathbf{V}^{sol} - \mathbf{V}^{com})$. Only the circulation is shown in the whole of the large box: the porous flow in 4.5d is uniform outside the small box and therefore the solid and liquid velocities are trivially related to the circulation velocity. The interpretation of the maximum amplitudes above each frame and the vector representation are all as in Figure 4.4b. The magmon ascent velocity for this case is 654×10^{-6} non-dimensional units. If circulation is not allowed, this magmon ascends at a velocity of 572×10^{-6}.

The liquid velocity 4.5a is larger than all the others and is largest within the magmon. The solid velocity 4.5b is more enlightening; here we see the dipole of compaction and dilation that allows the waveform to ascend. Comparing 4.5c and 4.4b, we see that the circulation is considerably modified when porous flow is permitted. The velocity at the peak of porosity is amplified and the vortices are now at the edge of the magmon. This pattern of circulation means that the advective (diapiric) component of the magmon ascent velocity is larger than that predicted from 4.4b, although it is small relative to the magmon velocity. In the porous flow field 4.5d we see the dipole from 4.5b without the superimposed circulation. The flow is uniform at the edges of the small box and is equal to the Darcy flow velocity corresponding to f_0. This plot shows that our small box is large enough to encompass all the variation in the porous flow field. This flow field looks very similar to the solid velocity when circulation is not permitted.

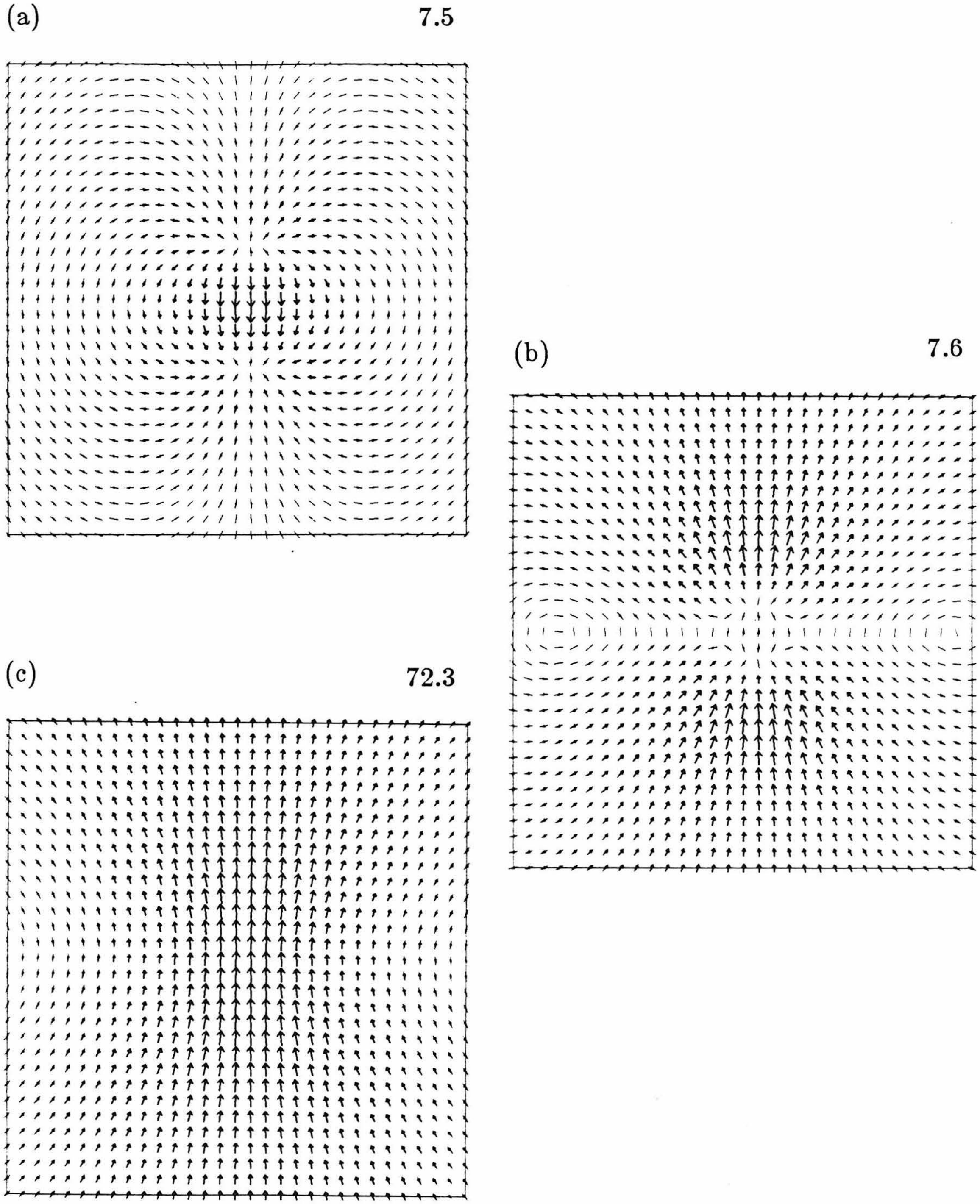

Figure 4.6. Solid velocity fields for (a) $\alpha = 3/7$, (b) $\alpha = 0.1$, and (c) $\alpha = 0.01$. The changes in the solid velocity field with decreasing α clearly show

the increased contribution of diapirism to the ascent of the magmon. 4.6a is the same as 4.5b, showing a dipole of compaction and dilation. In generating 4.6b and 4.6c, we again took an approximate magmon as the initial condition and ran it to steady state. In 4.6c, the shear viscosity is now low enough for the solid velocity to look very much like that for purely diapiric ascent. The dipole of compaction and dilation is still present, but it is obscured by the high amplitude circulation velocities. 4.6b shows a transitional case, where the solid velocity at the peak of the magmon is almost zero, a balance between upward circulation and downward motion between the poles of the dipole. The similarity in the amplitudes of 4.6a and 4.6b is misleading because of this cancellation.

The magmon ascent velocity corresponding to 4.6c is 725×10^{-6}. The increase relative to the value of 654×10^{-6} for 4.6a is due to more rapid diapiric ascent. The magmon retains its shape-preserving character despite the substantial contribution of a non-shape-preserving process to its ascent.

Analytic Form of Multi-Dimensional Solitary Waves

In Chapter 3 we were able to show a close correspondence between numerical experiments and analytical theory for the one-dimensional system. Despite the greater difficulty of analyzing the two-dimensional system, we are able to show that solitary waves of circular cross section should exist.

For historical reasons, and to clarify the method, we divide this analysis into two sections. First we treat the simplified system in which circulation is not allowed. The results from this analysis are used to guide the treatment of the full system of governing equations with circulation.

Analysis without circulation. We proceed by rewriting Equations (2.24a,b) and (2.27) in the approximate form

$$w = f^n \left[-1 + (1 - \alpha)\, f_{tz} + \alpha\, \nabla^2 w \right] \tag{4.2a}$$

$$u = f^n \left[(1 - \alpha)\, f_{tx} + \alpha\, \nabla^2 u \right] \tag{4.2b}$$

$$f_t = w_z + u_x \,. \tag{4.3}$$

Circulation, and the advective contribution to f_t, are omitted. We seek a solution to Equations (4.2a,b) and (4.3) in which the porosity takes the form of a propagating wave of circular cross section:

$$f\,(x, y, t) = \phi\,(\xi) \tag{4.4}$$

$$\xi^2 \equiv x^2 + y^2 \qquad y \equiv z - ct \,.$$

In a coordinate system ascending at velocity c, ξ is the radial coordinate centered on the peak of porosity. It then follows that

$$\mathrm{f_{tz}} = -\frac{\mathrm{c}}{\xi}\,\phi' - \frac{\mathrm{c\,y^2}}{\xi^3}\,(\xi\,\phi'' - \phi') \qquad (4.5\mathrm{a})$$

$$\mathrm{f_{tx}} = -\frac{\mathrm{c\,x\,y}}{\xi^3}\,(\xi\,\phi'' - \phi')\,, \qquad (4.5\mathrm{b})$$

where a prime denotes differentiation with respect to ξ. On comparison with Equations (4.2a,b), these suggest the following trial solutions for the velocity components:

$$\mathrm{w} = \omega\,(\xi) + \mathrm{y}^2\,\chi\,(\xi) \qquad (4.6\mathrm{a})$$

$$\mathrm{u} = \mathrm{x\,y}\,\chi\,(\xi)\,. \qquad (4.6\mathrm{b})$$

The symmetry of these forms is appropriate: w is even about the horizontal axis $y = 0$, and u is odd about both $y = 0$ and the vertical axis $x = 0$. The unknown functions $\phi\,(\xi)$, $\omega\,(\xi)$, and $\chi\,(\xi)$ are found to satisfy the following three coupled, non-linear ordinary differential equations:

$$\omega = \phi^{\mathrm{n}}\left[-1-(1-\alpha)\,\frac{\mathrm{c}}{\xi}\,\phi' + \alpha\left\{2\,\chi + \omega'' + \frac{1}{\xi}\,\omega'\right\}\right] \qquad (4.7\mathrm{a})$$

$$\chi = \phi^{\mathrm{n}}\left[(1-\alpha)\,\frac{\mathrm{c}}{\xi^3}\,(\phi' - \xi\,\phi'') + \alpha\left\{\chi'' + \frac{5}{\xi}\,\chi'\right\}\right] \qquad (4.7\mathrm{b})$$

$$-\frac{\mathrm{c}}{\xi}\,\phi' = \frac{1}{\xi}\,\omega' + 3\,\chi + \xi\,\chi'\,. \qquad (4.8)$$

Equation (4.8) is obtained by substitution of the trial solutions into (4.3). Substitution of (4.5a) and (4.6a) into (4.2a) gives an equation with terms involving only ξ, and terms that include y^2; separation of these two groups gives

Equations (4.7a) and (4.7b). This separation must be permissible if circular solutions, dependent only on ξ, are to exist. Substitution of (4.5b) and (4.6b) into (4.2b) duplicates Equation (4.7b), demonstrating that the above procedure is consistent. In axisymmetric cylindrical coordinates, the same analysis leads to a system of equations that differ from (4.7a,b) and (4.8) only in the value of certain of the numerical constants.

In either case, the circular solitary wave solution defined by the functions ϕ, ω, and χ may not be unique. However, we can show that solutions with elliptical cross sections ($\xi^2 \equiv x^2 + A\, y^2, A \neq 1$) do not exist. The analysis strongly suggests that the preferred solutions have circular cross sections in two dimensions, and spherical forms in three dimensions.

Analysis with circulation. In two-dimensional space, the analysis above leads to three unknown functions (ϕ, ω, χ) representing the porosity and two components of velocity. Introducing circulation allows two further degrees of freedom: the non-lithostatic pressure p^* and a scalar stream function ψ representing the circulation. (The letter ψ was used for an unrelated purpose in Chapters 1 and 3). The components of the circulation are given by

$$W = \psi_x \qquad U = -\psi_z \, . \tag{4.9}$$

The advantages of this representation are that the incompressibility of the circulation is satisfied automatically, and that the number of variables is reduced by one.

Consideration of the previous analysis and the numerical experiments suggests the following trial functions for the porosity, the porous flow field, the pressure, and the stream function.

$$f = \phi\,(\xi) \tag{4.10}$$

$$w - W = \omega\,(\xi) + y^2\,\chi\,(\xi) \tag{4.11a}$$

$$u - U = x\,y\,\chi\,(\xi) \tag{4.11b}$$

$$p^* = y\,\pi\,(\xi) \tag{4.12}$$

$$\psi = x\,\kappa\,(\xi)\,. \tag{4.13}$$

The motivation for these choices is as follows.

1. We observe circular porosity profiles in the numerical experiments.
2. The pattern of porous flow in the numerical experiments with circulation (Figure 4.5d) closely resembles the solid velocity in those without circulation. The forms in (4.11a,b) are taken directly from (4.6a,b)
3. The pressure field in (4.12) is a dipole, corresponding to the pattern of compaction and dilation that we expect.
4. The circulation represented by this stream function (4.13) has the general form and symmetry of the pattern in Figure 4.5c. As usual, the streamlines of the flow are the contours of the stream function.

Substitution of these trial functions into the governing equations does indeed produce a set of five coupled ordinary differential equations in which only the radial coordinate ξ and the five functions ϕ, ω, χ, π, and κ, appear. Starting with Darcy's law (2.24a,b), the Stokes equation (2.25a,b) and the equation for compaction (2.27), we obtain the following equations.

$$\omega = \phi^{\mathrm{n}} \left[- (1 - \phi) + (1 - \alpha) \left(\frac{1}{\xi} (\omega' + \chi') + 3\, \chi \right) + \alpha \left(\omega'' + 2\, \chi + + 4\, \kappa'' + \xi\, \kappa''' \right) \right] \tag{4.14a}$$

$$\chi = \phi^{\mathrm{n}} \left[(1 - \alpha) \left(\frac{1}{\xi^2} (\omega'' + \chi'') - \frac{1}{\xi^3}\, \omega' + \left\{ \frac{3}{\xi} - \frac{1}{\xi^3} \right\} \chi' \right) + \alpha \left(\chi'' + \frac{5}{\xi}\, \chi' + \frac{3}{\xi^3}\, \kappa' - \frac{3}{\xi^2}\, \kappa'' - \frac{1}{\xi}\, \kappa''' \right) \right] \tag{4.14b}$$

$$\alpha \left(4\, \kappa'' + \xi\, \kappa''' \right) - \pi = - \phi - \left[(1 - \alpha) \left(\frac{1}{\xi} (\omega' + \chi') + 3\, \chi \right) + \alpha (\omega'' + 2\, \chi) \right] \tag{4.15a}$$

$$\alpha \left(\frac{3}{\xi^3}\, \kappa' - \frac{3}{\xi^2}\, \kappa'' - \frac{1}{\xi}\, \kappa''' \right) - \frac{1}{\xi}\, \pi' = - \left[(1 - \alpha) \left(\frac{1}{\xi^2} (\omega'' + \chi'') - \frac{1}{\xi^3}\, \omega' + \left\{ \frac{3}{\xi} - \frac{1}{\xi^3} \right\} \chi' \right) + \alpha \left(\chi'' + \frac{5}{\xi}\, \chi' \right) \right] \tag{4.15b}$$

$$- \frac{\mathrm{c}}{\xi}\, \phi' = (1 - \phi) \left(\frac{1}{\xi}\, \omega' + 3\, \chi + \xi\, \chi' \right) - \phi' \left(\frac{1}{\xi} (\omega - \kappa) + \xi\, \chi \right) \tag{4.16}$$

No approximations, e.g., $\phi << 1$, have been made in obtaining these equations. They demonstrate quite generally that waves of circular form should exist. This conclusion is independent of the viscosity parameter α, which is perhaps surprising as materials with very different resistances to shear and compaction might be expected to produce waves with significant differences. As it appears, a change in α affects the functions ϕ, ω, χ, ψ, and κ, but does not introduce any non-radial dependence of these functions.

The permeability function, represented by ϕ^{n} in (4.14a,b), can probably take any form, as long as it is isotropic and non-zero for all values of $\phi > 0$. If the permeability is removed in equations (4.14a,b) the whole system of equations breaks down. Physically, this implies that solitary waves of porosity are not expected to arise in buoyancy-driven circulation without porous flow.

When the analysis with circulation is repeated with axisymmetric cylindrical coordinates a similar set of equations is obtained, describing a spherical waveform. A numerical dispersion relation for two- and three-dimensional solitary waves, like the analytic form for one-dimensional waves derived in Chapter 3, could be obtained by direct solution of Equations (4.14a,b), (4.15a,b), and (4.16). This would not provide any new physical insight, but it would provide a useful check on the numerical experiments above in which solitary wave solutions were not required *a priori*.

The key to performing this analysis is the correct choice of velocity variables. It would be very difficult to guess the correct functional forms for, e.g., the solid and liquid velocities. For example, we can show from Equations (4.9), (4.11) and (4.13) that the vertical component of the solid velocity w has the form $\omega + \kappa + y^2 \chi + x^2 \kappa' / \xi$.

Discussion: The Competition between Porous Flow and Circulation

A significant advantage of partitioning the flow as we have done is that we can conveniently address problems of porous flow in a partially molten region that is embedded in the circulating mantle. The porous flow will be confined to this region; it is driven by the buoyancy of the liquid and by the large scale hydrodynamic pressure gradients associated with the circulation. The circulation field will cross the boundaries of the region in a continuous fashion. Within the region, it is driven by the distribution of buoyancy and by the externally imposed flows at the boundaries.

Consider a situation in which there is no externally imposed circulation in the region. Reiterating, a localized region of porosity could ascend as a diapir (solid and liquid together) or as a magmon (segregation of solid and liquid). The Stokes ascent velocity v_d of a spherical diapir of radius r_d, omitting a constant of order unity, is as follows.

$$v_d \sim \frac{g\,\Delta\rho}{\eta}\, r_d^2\,(f_{max} - f_0) \tag{4.17}$$

This can be expressed in non-dimensional form, using the dimensional scales given in Table 3.1. We also assume $f_{max} >> f_0$.

$$\frac{v_d}{V} \sim \left(\frac{r_d^2}{L^2}\right)\frac{f_{max}}{\alpha} \tag{4.18}$$

From the analysis of one-dimensional waves in Chapter 3, the ascent velocity v_m of a magmon with the same peak and background porosities is given approximately by

$$\frac{v_m}{V} \sim 2\, f_0\, f_{max}\,. \tag{4.19}$$

We have assumed that $n = 3$ and $m = 0$, as usual. Because the balance of forces that determines this ascent velocity is essentially the same in one and three dimensions, we use (4.19) to approximate the velocity of a spherical magmon. The corresponding magmon radius r_m is given by

$$\frac{r_m}{L} \sim 2\, f_0^{1/2}\, f_{max}\,. \tag{4.20}$$

Herein lies an important difference between magmons and diapirs. The size of a magmon is internally determined by the material properties and the peak and background porosities. A diapir can have any radius r_d that we choose.

If we set $r_d = r_m$, then it follows from (4.18), (4.19), and (4.20) that

$$\frac{v_d}{v_m} \sim 2\,\frac{f_{max}^2}{\alpha}\,. \tag{4.21}$$

Since $f_{max} << 1$, this equation shows that, on the size scale of magmons, diapiric ascent can compete only if α is small. The effect of reducing α is illustrated in Figure 4.6.

We are at liberty to choose a larger value of r_d. The ascent velocity increases as the square of the radius, so that a sufficiently large diapir will ascend more quickly than a magmon specified by the same porosities. Below we argue that magmons will still form from, and ascend relative to, such a diapir.

The pattern of circulation caused by the large diapir will be similar to that shown in Figure 4.4b. The localized region of buoyancy carries up the background material in its vicinity, particularly above and below. To a good approximation, the region around the diapir is undergoing a Galilean transformation, i.e., a uniform translation upward. Darcy's law is invariant under such a transformation, so that the familiar processes of porous flow and compaction will proceed in this ascending frame of reference.

At this point we refer to the one-dimensional calculation shown in Figure 4.7. The initial state is intended to represent a vertical profile through the peak of the diapir, with the frame of reference for the whole calculation undergoing ascent. We conclude that a large diapir will break down into a "school" of magmons. The school gradually spreads out, but while it remains localised the combined buoyancy continues to contribute a substantial diapiric ascent

Text continues on page 87

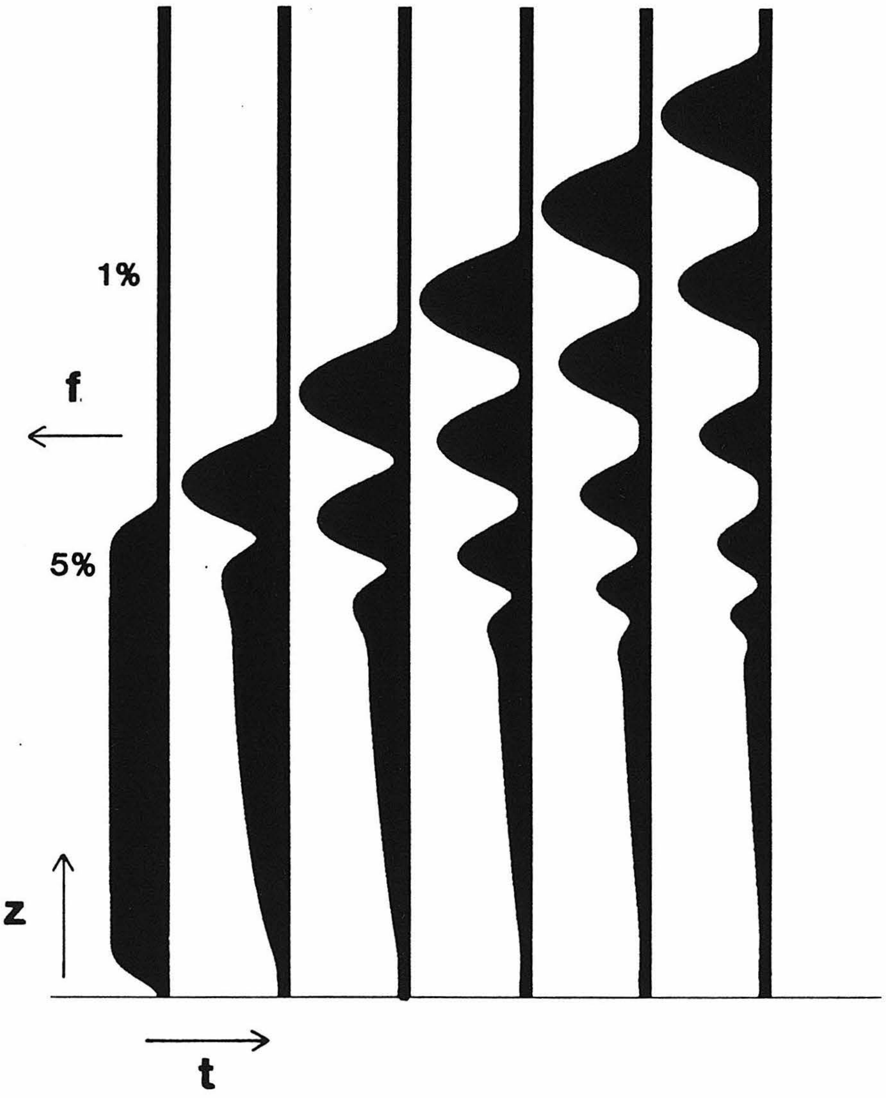

Figure 4.7. Development of solitary waves from a larger region of high porosity. The high porosity region in the initial state is larger than the wavelength of a wave with the same peak and background porosity. The region breaks up into a rank-ordered train of solitary waves. This calculation uses m = 0 and n = 3, as in Figure 3.2. Here, the wave amplitudes are lower and the deviation from a parabolic profile at the edges of the waves is more apparent.

velocity.

An alternative statement of this conclusion is that, within a partially molten region, the length scale of the appropriate magmon will always be superimposed on variations with longer length scales. The most probable source of a longer length scale variation would be the Rayleigh-Taylor instability of a basal layer of high porosity, perhaps supplied by melting at depth. Whitehead *et al.* [1985] propose that such an instability leads to the separation of volcanic centers along midocean ridges. While not endorsing this model, we note that their geometry would also give rise to magmons in the manner described above.

An interesting corollary to the discussion of diapiric ascent arises because, in the Earth, upward circulation will cause melting due to pressure release. For example, the pattern of circulation for an individual magmon, shown in Figure 4.5c, will cause some additional melting in the region of the magmon. We calculate that the rate of amplification in the amplitude of the magmon due to this melting will very small. For the larger diapirs that we have discussed, the melting due to the higher rate of upward circulation may modify the magmons that develop. The pattern of melting will be pervasive; i.e., melting will occur both in the magmons and in the background. As we discussed in Chapter 3, this pattern will tend to degrade the magmons.

The preceding discussion lends some insight into the internal dynamics of a partially molten region. We may now wish to include a pattern of circulation driven from the exterior of the region. The system is now more complicated because we cannot ignore the pattern of melting caused by the circulation, due to pressure release. To understanding the behavior of such as system we must return to numerical modeling. The type of calculation called for would involve both partially molten and unmelted regions. For example, we could investigate the flow in the partially molten asthenosphere and solid mantle underlying a spreading ridge, hot spot, or subduction zone. Darcy's law governs porous flow only in the regions with melt; the Stokes equation governs circulation everywhere, with the interaction term **A** included where porous flow is occurring. With the addition of pressure-release melting and the use of a realistic geometry such a calculation may provide a realistic model of processes in the Earth. The magmon calculations with circulation presented above, in addition to their intrinsic interest, represent a preparatory step towards these calculations.

APPENDIX

NUMERICAL METHODS

Porous Flow in One Dimension

Representative of the equations we wish to solve for the porosity f and solid velocity w are the following.

$$w = f^3 [-1 + w_{zz}] \tag{A1}$$

$$f_t = w_z \tag{A2}$$

The one-dimensional material is broken up into N elements of equal size δz, separated by N+1 nodes. The porosity profile is discretized by specifying a value for each element. The velocity field is specified at the nodes.

The first part of the algorithm is the solution of the boundary value problem (A1). Physically, we wish to determine the velocity field due to a given distribution of porosity. For each node point i the equation is written in discretized form.

$$w^i = (f^i)^3 \left[-1 + \frac{w^{i+1} - 2\,w^i + w^{i-1}}{\delta z^2} \right] \tag{A3}$$

The porosity value f^i is obtained by interpolation between the adjoining elements. A second order finite-difference approximation for w_{zz} has been used. At the boundary nodes ($i = 0, N+1$), suitable boundary conditions are used; e.g., $w^0 = 0$ or $w^0 = w^1$. The resulting set of N+1 equations can be represented by a tridiagonal linear system, which is easily solved for the N+1 unknown values of velocity w^i.

The second part of the algorithm is the advancement of the porosity profile f in time. The time derivative f_t for an element j is obtained directly using the discretized form of (A2).

$$f_t^j = \frac{w^{i+1} - w^i}{\delta z} \tag{A4}$$

The nodes i and i+1 border the element j.

This value of f_t^j is correctly centered in space but lies at the beginning of a time step rather than at the middle. In a fashion related to the Lax-Wendroff method (see Press *et al.* [1986]), we advance f from time t to time $t + {}^1/_2\ \delta t$ using the uncentered values of f_t. The solution of Equations (A3) and (A4) is then repeated to obtain a better estimate for the time derivative centered between t and $t + \delta t$. This procedure is iterated until the centered estimates of f_t converge, at which point f is advanced to time $t + \delta t$.

For solitary waves, the time step δt is chosen to satisfy the Courant condition, i.e., $\delta t < \delta z / c$, where c is the phase velocity. In order to accelerate the convergence of the iterative scheme, we exploit the translational invariance of the solitary wave to estimate the porosity profile at time $t + {}^1/_2\ \delta t$ before the initial calculation of w.

Porous Flow in Two Dimensions

We now wish to solve three equations in the three variables f, w, and u. For example,

$$w = f^3\left(- 1 + w_{zz} + {}^3\!/_7\, w_{xx} + {}^4\!/_7\, u_{xz}\right) \qquad \text{(A5a)}$$

$$u = f^3\left(u_{xx} + {}^3\!/_7\, u_{zz} + {}^4\!/_7\, w_{zx}\right) \qquad \text{(A5b)}$$

$$f_t = w_z + u_x\,. \qquad \text{(A6)}$$

The two-dimensional medium is now tessellated by square elements, with nodes at each corner. The porosity is defined in the elements, and the velocities at the nodes.

Again, the first part of the algorithm solves Equations (A5a,b) for the velocity field, given the porosity distribution. We solve (A5a) for the vertical velocity w and (A5b) for the lateral velocity u, using a form of the alternating direction implicit finite-difference method (see Press *et al.* [1986]). In this method, the equations are solved in a series of iterative steps. In each set of four steps, each equation is solved in each direction.

For example, in solving (A5a) in the z-direction, we solve for w and w_{zz}, estimating for the remaining terms using the most recent values of the velocity field. This solution is performed for every column of nodes.

Each step in the solution is equivalent to a series of one-dimensional boundary value problems, the solution of which is described in the preceding section. The sets of four steps are repeated until the values of velocity converge. As before, we use second-order estimates of the derivatives and interpolate between elements to obtain values for the porosity at the nodes.

The advancement of f in time is accomplished in exactly the same way as in the one-dimensional case. We calculate the divergence of the velocity field, on the RHS of (A6), using the velocities at the four nodes surrounding an element. The time derivative f_t is again correctly centered in space. The same iterative procedure is used to center f_t in time. Note that we have two iterative loops; one for evaluating the velocity field, and one for centering in time. In practice these are intertwined for more rapid convergence. For solitary waves, we can decrease the calculation time by starting each time step with a good estimate of the porosity profile and velocity field at time $t + {}^1/_2\ \delta t$.

Experiments shown in Figures 4.1, 4.2, and 4.3. The element size was chosen after we studied the exact analytic solution for the one-dimensional case, and in light of the experiments on the one-dimensional system. The minimum size that can be used is controlled by the sharpness of the transition between the uniform background region and the main body of the waveform. An accurate solution can be obtained by using a node spacing equal to the compaction length for the background porosity [McKenzie, 1984; Scott and Stevenson, 1984]. For a background porosity of 1%, and with $n = 3$ and $m = 0$, the compaction length is 10^{-3}. This node spacing was used for the experiments in Figures 4.1, 4.2, and 4.3. In both the Cartesian and cylindrical cases the lateral and vertical element dimensions are equal. The time step was chosen with reference to the maximum phase velocity expected to arise during the experiment, as in the one-dimensional case. These experiments each took roughly 3 hours on a VAX 11/780.

We performed all these calculations using a scrolling grid, in order to keep the solitary waves away from the top and bottom edges of the grid while minimizing computational time. The equations were not, however, solved in a moving frame of reference. The scrolling is accomplished by our adding a new row of elements at the top of the grid between time steps and removing a row from the bottom. The new elements all have $f = f_0$, the background porosity.

This procedure is justified because we always ensure that non-uniform regions of porosity do not approach the edges of the grid.

The accuracy of the calculations have been assessed by our repeating certain examples with different element sizes and time steps. First, we have studied the effects of these changes on the solitary waves used in the initial state of Figure 4.2. We note the following:

1. Solitary waves that propagate for many wavelengths with changes in the waveform of less than 1 part in 10^4 are always produced after some transient adjustment.

2. Halving the time step (from the maximum permitted by the velocity of the wave) changes the wave amplitude by less than 0.1%.

3. Halving the element size (by interpolating), and the time step, changes the wave amplitude by less than 0.5%.

The measured phase velocity also changes slightly. We expect some changes, corresponding to the changes in wave amplitude; the observed changes are comparable to those predicted from the dispersion relation for one-dimensional solitary waves.

Second, we have repeated the calculation shown in Figure 4.2a with a halved element size and time step. The phase shift of the larger wave that arises through the collision with the smaller wave changes by less than 2%. Errors in the phase shift would accumulate through the several hundred time steps performed, so we consider this to be a searching test of the method.

Porous Flow and Circulation in Two Dimensions

The qualitative description of the method in the caption to Figure 4.4 serves as an introduction to this section. The equations, reproduced from Chapter 2, are as follows.

- Darcy's Law

$$\mathrm{w} - \mathrm{W} = \mathrm{f}^{\mathrm{n}} \left[-(1-\mathrm{f}) + \mathrm{w}_{\mathrm{zz}} + \alpha\, \mathrm{w}_{\mathrm{xx}} + (1-\alpha)\, \mathrm{u}_{\mathrm{xz}} \right] \tag{2.24a}$$

$$\mathrm{u} - \mathrm{U} = \mathrm{f}^{\mathrm{n}} \left[\mathrm{u}_{\mathrm{xx}} + \alpha\, \mathrm{u}_{\mathrm{zz}} + (1-\alpha)\, \mathrm{w}_{\mathrm{xz}} \right] \tag{2.24b}$$

- Stokes Equation

$$\alpha(\mathrm{W}_{\mathrm{zz}} + \mathrm{W}_{\mathrm{xx}}) - \mathrm{p}_{\mathrm{z}}^{*} = \tag{2.25a}$$

$$- \mathrm{f} - \left[(\mathrm{w}-\mathrm{W})_{\mathrm{zz}} + \alpha\, (\mathrm{w}-\mathrm{W})_{\mathrm{xx}} + (1-\alpha)\, (\mathrm{u}-\mathrm{U})_{\mathrm{xz}} \right]$$

$$\alpha(\mathrm{U}_{\mathrm{zz}} + \mathrm{U}_{\mathrm{xx}}) - \mathrm{p}_{\mathrm{x}}^{*} = - \left[(\mathrm{u}-\mathrm{U})_{\mathrm{xx}} + \alpha\, (\mathrm{u}-\mathrm{U})_{\mathrm{zz}} + (1-\alpha)\, (\mathrm{w}-\mathrm{W})_{\mathrm{xz}} \right] \tag{2.25b}$$

- Continuity

$$\mathrm{W}_{\mathrm{z}} + \mathrm{U}_{\mathrm{x}} = 0 \tag{2.26}$$

- Compaction

$$\mathrm{f}_{\mathrm{t}} = (1-\mathrm{f})\, (\mathrm{w}_{\mathrm{z}} + \mathrm{u}_{\mathrm{x}}) - (\mathrm{w}\, \mathrm{f}_{\mathrm{z}} + \mathrm{u}\, \mathrm{f}_{\mathrm{x}}) \tag{2.27}$$

The basic structure of the solution remains the same; we solve a boundary value problem for the velocity fields due to a given distribution of porosity, and then advance the porosity in time. The details of the method described here are tuned to the specific problem of a solitary wave in a large, uniform region. The porous flow field (w – W, u – U) and the circulation (W, U) have physically different characters; this contrast leads us to divide up the region into small square elements around the wave and large elements away from the wave. The small box so defined is of comparable size to the boxes used for the experiments without circulation. As shown schematically in Figure 4.4a, the elements outside the small box have different shapes in different parts of the region. As before, the porosity is defined in the elements, and both velocity fields are defined at the nodes.

The boundary value problem for the velocity fields is now more complex and is divided into two parts. The solution of the Stokes equation (2.25a,b) is intertwined with the solution of Darcy's law (2.24a,b) in an iterative scheme.

Darcy's law is solved for the solid velocity field in the small box only. The components of the circulation (W, U) are included, but they are treated as known quantities. Given the distribution of porosity and the most recent estimate of the circulation, the solid velocity is obtained exactly as it was without circulation.

We solve the Stokes equation for the circulation and pressure in the entire region, subject to the incompressibility constraint (2.26). Because of the irregular shapes of the elements, the finite-element method is ideal for this purpose. We have adapted an existing thermal convection simulator (A. Raefsky and B. Hager, personal communication) which uses augmented Lagrangian algorithm to solve the penalty formulation of Stokes flow. In this formulation the fluid is compressible, but has a very low compressibility. We prescribe the buoyancy distribution due to porosity and the interaction term **A** represented by the remaining terms on the RHS of (2.25a,b). The algorithm calculates the resulting pattern of circulation, which is divergence-free to high accuracy. The pressure field is also obtained, although it is of no use elsewhere.

Combining these very different methods of solution into a hybrid iterative scheme requires some care. It is important that the circulation field used, when we are solving Darcy's law, is divergence-free: otherwise, anomalous compaction processes will occur. It is also important that we do obtain a good solution for the porous flow between calls to the circulation solver. Then we can guarantee that the interaction term **A** is zero when summed over the small box, and so no anomalous buoyancy is generated. With these provisions, the iterative scheme works remarkably well, considering its cumbersome appearance.

The advancement of f in time is accomplished much as before, with the iterative scheme for centering intertwined with the solutions for the velocity fields. Note that the equation used (2.27) now has an advective contribution (the latter terms on the RHS). While the pattern of elements and nodes is ideal for calculating the compaction terms, it does not provide a good framework for calculating the advection terms. This is a familiar problem in convection calculations (where temperature is advected) and can certainly be overcome. For the present, it is the need for the incorporation of a stable advective scheme that sets a lower limit on the value of α used in the magmon experiments. At lower values of α, the advective contribution to the ascent velocity becomes dominant and instabilities develop in the numerical scheme.

Other drawbacks of the numerical scheme as a whole arise because of its hybrid nature. These were discovered in attempts to repeat the magmon experiments in axisymmetric cylindrical coordinates. These experiments are of interest because they simulate three dimensions. The ascent velocity of a diapir in an infinite medium is well defined in three dimensions (Equation (4.17)), but in two dimensions it diverges. In practice, the velocity depends on the size of the box representing the infinite medium.

These attempts have failed because of two differences between the finite difference and finite element representations of the governing differential equations. First, the way that the divergence of the circulation field is calculated is slightly different in cylindrical coordinates. Consequently, the porous flow is superimposed on a circulation field that is not quite incompressible. Second, the singular point at r = 0 is handled differently by the two methods. The finite difference method solves the differential equation at the nodes at r = 0, using asymptotic forms for the singular terms. The finite element method solves the equation in the element adjacent to r = 0, but not at r = 0; the asymptotic forms are not needed. These problems could be overcome, but it is probably more appropriate to develop a full finite element scheme.

References

Arzi, A. A., Critical phenomena in the rheology of partially molten rocks, *Tectonophysics*, **44**, 173-184, 1978.

Auer, F., H. Beckmeimer, and G. Oehlschlegel, Steady-state creep of fine grain granite at partial melting, *J. Geophys.*, **49**, 89-92, 1981.

Barcilon, V., and F. M. Richter, Non-linear waves in compacting media, *J. Fluid. Mech.*, **164**, 429-448, 1986.

Bear, J., *Dynamics of Fluids in Porous Media*, 764pp., American Elsevier, New York, 1972.

Beeré, W., A unifying theory of the stability of penetrating liquid phases and sintering pores, *Acta Metall.*, **23**, 131-138, 1975.

Carman, P. C., Fluid flow through granular beds, *Trans. Inst. Chem. Eng.*, **15**, 150-161, 1937.

Cooper, R. F., and D. L. Kohlstedt, Rheology and structure of olivine-basalt partial melts, *J. Geophys. Res.*, **91**, 9315-9323, 1986.

Cooper, R. F., and D. L. Kohlstedt, Solution-precipitation enhanced diffusional creep of partially molten olivine-basalt aggregates during hot-pressing, *Tectonophysics*, **107**, 207-233, 1984.

Drazin, P. G., *Solitons*, 136pp., London Mathematical Society Lecture Notes Series 85, Cambridge University Press, 1983.

Drew, D. A., Averaged field equations for two-phase media, *Stud. Appl. Math.*, **50**, 133-166, 1971.

Dullien, F. A. L., *Porous Media Fluid Transport and Pore Structure*, Academic Press, New York, 1979.

Fornberg, B. and G. B. Witham, A numerical and theoretical study of certain non-linear wave phenomena, *Phil. Trans. R. Soc. London*, **289**, 373-404, 1978.

Fowler, A. C., A mathematical model of magma transport in the asthenosphere, *Geophys. Astrophys. Fluid Dynamics*, **33**, 63-96, 1985.

Fowler, A. C., On the transport of moisture in polythermal glaciers, *Geophys. Astrophys. Fluid Dynamics*, **29**, 99-140, 1984.

Harris, P. G., Zone refining and the origin of potassic basalts, *Geochim. Cosmochim. Acta*, **12**, 195-208, 1957.

Huppert, H. E., R. S. J. Sparks, J. A. Whitehead, and M. A. Hallworth, The replenishment of magma chambers by light inputs, *J. Geophys. Res.*, **91**, 6113-6122, 1986.

Jurewicz, S. R., and A. J. G. Jurewicz, Distribution of apparent angles on sections with emphasis on dihedral angle measurements, *J. Geophys. Res.*, **91**, 9277-9282, 1986.

Jurewicz, S. R., and E. B. Watson, The distribution of partial melt in a granitic system: The application of liquid phase sintering theory, *Geochim. Cosmochim. Acta.*, **49**, 1109-1121, 1985.

Kushiro, I., Viscosity of partial melts in the upper mantle, *J. Geophys. Res.*, **91**, 9343-9350, 1986.

Maaløe, S., and A. Scheie, The permeability-controlled accumulation of primary magma, *Contrib. Mineral. Petrol.*, **81**, 350-357, 1982.

McKenzie, D. P., ^{230}Th–^{238}U disequilibrium and the melting process beneath ridge axes, *Earth Planet. Sci. Lett.*, **72**, 149-157, 1985.

McKenzie, D. P., The extraction of magma from the crust and mantle, *Earth Planet. Sci. Lett.*, **74**, 81-91, 1985.

McKenzie, D. P., The generation and compaction of partial melts, *J. Petrol.*, **25**, 713-765, 1984.

Navon, O, and E. M. Stolper, Geochemical consequences of melt percolation: The upper mantle as a chromatographic column, *J. Geology*, in press, 1986.

Nye, J. F., The flow law of ice from measurements in glacier tunnels, laboratory experiments and the Jungfraufirn borehole experiment, *Proc. R. Soc. London*, **A219**, 477-489, 1953.

O'Hara, M., Importance of the "shape" of the melting regime during partial melting of the mantle, *Nature*, **314**, 58-62, 1985.

Olson, P., G. Schubert, and C. Anderson, Plume formation in the D$''$ -layer and the roughness of the core-mantle boundary, submitted to *Nature*, 1986.

Olson, P., and U. Christensen, Solitary wave propagation in a fluid conduit within a viscous matrix, *J. Geophys. Res.*, **91**, 6367-6374, 1986.

Press, W. H., B. P. Flannery, S. A. Teukolsky, and W. T. Vetterling, *Numerical Recipes*, 818pp, Cambridge University Press, Cambridge, 1986.

Prestwich, J., On the agency of water in volcanic eruptions; with some observations on the thickness of the Earth's crust from a geological point of view; and on the primary cause of volcanic action, *Proc. R. Soc. London*, **38**, 253-260, 1885.

Ribe, N., The generation and compaction of partial melts in the Earth's mantle, *Earth Planet. Sci. Lett.*, **73**, 361-376, 1985.

Richter, F. M., and D. P. McKenzie, Dynamical models for melt segregation from a deformable matrix, *J. Geol.*, **92**, 729-740, 1984.

Rigden, S. M., T. J. Ahrens, and E.M. Stolper, Densities of silicate liquids at high pressures, *Science*, **226**, 1071-1074, 1984.

Scott, D. R., and D. J. Stevenson, Magma ascent by porous flow, *J. Geophys. Res.*, **91**, 9283-9296, 1986.

Scott, D. R., and D. J. Stevenson, Magma solitons, *Geophys. Res. Lett.*, **11**, 1161-1164, 1984.

Scott, D. R., D. J. Stevenson, and J. A. Whitehead, Jr., Observations of solitary waves in a viscously deformable pipe, *Nature*, **319**, 759-761, 1986.

Shaw, H. R., The fracture mechanisms of magma transport from the mantle to the surface, in *Physics of Magmatic Processes*, edited by R. B. Hargraves, pp.

201-264, Princeton University Press, Princeton, N.J., 1980.

Sleep, N. H., Segregation of a magma from a mostly crystalline mush, *Geol. Soc. Am. Bull.*, **85**, 1225-1232, 1974.

Spence, D. A. and D. L. Turcotte, Magma driven propagation of cracks, *J. Geophys. Res.*, **90**, 575-580, 1985.

Spera, F. J., Carbon dioxide in petrogenesis, III, Role of volatiles in the ascent of alkaline magmas with special reference to xenolith bearing mafic lavas, *Contrib. Mineral. Petrol.*, **88**, 217-232, 1984.

Stevenson, D. J., On the role of surface tension in the migration of melts and fluids, *Geophys. Res. Lett.*, **13**, 1149-1152, 1986.

Stevenson, D. J., and D. R. Scott, Melt migration in deformable media, NATO ASI Series, Proceedings of the Workshop on the Structure and Dynamics of Partially Solidified Systems, 1987.

Stevenson, D. J., Magmatic transport by the migration of fluid-filled cracks, *Trans. Am. Geophys. Un. EOS*, **64**, 848, 1983.

Stevenson, D. J., Self-regulation and melt migration (can magma oceans exist?), *Trans. Am. Geophys. Un. EOS*, **61**, 1021, 1980.

Stolper, E., D. Walker, B. H. Hager, and J. F. Hays, Melt segregation from partially molten source regions: the importance of melt density and source region size, *J. Geophys. Res.*, **86**, 6261-6271, 1981.

Toramaru, A., and N. Fujii, Connectivity of the melt phase in partially molten peridotite, *J. Geophys. Res.*, **91**, 9239-9252, 1986.

Turcotte, D. L., Magma migration, *Ann. Rev. Earth Planet. Sci.*, **10**, 397-408, 1982.

Turcotte, D. L., and J. L. Ahern, A porous flow model for magma migration in the asthenosphere, *J. Geophys. Res.*, **83**, 767-772, 1978.

Vaughan, P. J., D. J. Kohlstedt, and H. S. Waff, Distribution of the glass phase in hot-pressed, olivine-basalt aggregates: An electron microscopy study, *Contrib. Mineral. Petrol.*, **81**, 253-261, 1982.

von Bargen, N., and H. S. Waff, Permeabilities, interfacial areas and curvatures of partially molten systems: Results of numerical computations of equilibrium microstructures, *J. Geophys. Res.*, **91**, 9261-9276, 1986.

Waff, H. S., Effects of the gravitational field on liquid distribution in partial melts within the upper mantle, *J. Geophys. Res.*, **85**, 1815-1825, 1980.

Waff, H. S., and J. R. Bulau, Equilibrium fluid distribution in an ultramafic partial melt under hydrostatic stress conditions, *J. Geophys. Res.*, **84**, 6109-6114, 1979.

Weertman, J., Theory of fluid-filled crevasses in glaciers applied to vertical magma transport beneath ridges, *J. Geophys. Res.*, **76**, 1171-1183, 1971.

Whitehead, J. A., and K. Helfrich, The Korteweg-de Vries equation from laboratory conduit and magma migration equations, *Geophys. Res. Lett.*, **13**, 545-546, 1986.

Whitehead, J. A., H. J. B. Dick and H. Schouten, A mechanism for magmatic accretion under spreading centres, *Nature*, **312**, 146-148, 1985.

Whitehead, J. A., and D. S. Luther, Dyanamics of laboratory diapir and plume models, *J. Geophys. Res.*, **80**, 705-717, 1975.

Whitehead, J. A., Instabilities of fluid conduits in a flowing earth - are plates lubricated by the asthenosphere? *Geophys. J. R. Astr. Soc.*, **70**, 415-433, 1982.

Wickham, S. M., The segregation and emplacement of granitic magmas, *J. G. S. London*, in press, 1987.